applied sciences

IMPACT FACTOR 2.5

CITESCORE 5.3

Article

Demystifying Quantum Gate Fidelity for Electronics Engineers

Mattia Borgarino and Alessandro Badiali

Special Issue

Low-Power Integrated Circuit Design and Application

Edited by

Dr. Anindita Paul and Prof. Dr. Jaime Ramirez-Angulo

MDPI

https://doi.org/10.3390/app15052675

applied sciences

MDPI

Article

Demystifying Quantum Gate Fidelity for Electronics Engineers

Mattia Borgarino [1,2,*] and Alessandro Badiali [1,3]

[1] Enzo Ferrari Engineering Department, University of Modena and Reggio Emilia, 41125 Modena, Italy; alessandro.badiali01@universitadipavia.it
[2] Consorzio Nazionale Interuniversitario per le Telecomunicazioni (CNIT), 43124 Parma, Italy
[3] Department of Electrical, Computer and Biomedical Engineering, University of Pavia, 27100 Pavia, Italy
* Correspondence: mattia.borgarino@unimore.it

Abstract: The implementation of quantum gates by means of microwave cryo-RFICs controlling qubits is a promising path toward scalable quantum processors. Quantum gate fidelity quantifies how well an actual quantum gate produces a quantum state close to the desired ideal one. Regrettably, the literature usually reports on quantum gate fidelity in a highly theoretical way, making it hard for RFIC designers to understand. This paper explains quantum gate fidelity by moving from Shannon's concept of fidelity and proposing a detailed mathematical proof of a valuable integral formulation of quantum gate fidelity. Shannon's information theory and the simple mathematics adopted for the proof are both expected to be in the background of electronics engineers. By using Shannon's fidelity, this paper rationalizes the integral formulation of quantum gate fidelity. Because of the simple mathematics adopted, this paper also demystifies to electronics engineers how this integral formulation can be reduced to a more practical algebraic product matrix. This paper makes evident the practical utility of this matrix formulation by applying it to the specific examples of one- and two-qubit quantum gates. Moreover, this paper also compares mixed states, entanglement fidelity, and the error rate's upper bound.

Keywords: fidelity; quantum fidelity; RFICs; quantum gate; hyperspace integrals; energy efficiency; logical qubit

Academic Editor: Alessandro Lo Schiavo

Received: 29 January 2025
Revised: 28 February 2025
Accepted: 28 February 2025
Published: 2 March 2025

Citation: Borgarino, M.; Badiali, A. Demystifying Quantum Gate Fidelity for Electronics Engineers. *Appl. Sci.* **2025**, *15*, 2675. https://doi.org/10.3390/app15052675

1. Introduction

A scalable and fault-tolerant quantum processor is the enabling device for the second quantum revolution, which, exploiting the counter-intuitive laws of quantum mechanics, promises to revolutionize, in the near-medium future, how information is processed and transmitted, with relevant impacts in several practical fields, such as cryptography, drug synthesis, and artificial intelligence [1].

Microelectronic technologies seem to assure scalability. In particular, cryogenic RFICs (radio frequency integrated circuits) are a promising solution for scaled quantum microprocessors [2–21]. The application of a microwave pulse with an appropriate amplitude, frequency, and time duration to a two-level quantum physical system (quantum bit or qubit for short) indeed enables the implementation of one-qubit quantum gates; likewise, two-qubit quantum gates can be implemented by applying suitable microwave pulses to a pair of qubits [22]. The useful frequency range spans from 100 MHz to 50 GHz for electron spin qubits and from 500 MHz to 15 GHz for superconductive qubits [23]. RFICs are interesting because they are microminiaturized microwave sources that can be placed close to the qubits, minimizing the number of microwave cables connecting the quantum microprocessor to the external room temperature environment. In this way, the size of the whole system is reduced and the adiabaticity of the cryostat is improved.

On the one hand, microelectronic technologies seem to assure scalability. However, on the other hand, the intrinsic brittle coherence of quantum objects constitutes the main challenge to achieving fault tolerance because it tends to increase the quantum computation error. The quantum error rate is the correct figure of merit for evaluating the fault-tolerance degree of a quantum processor [24]. An important theorem of quantum information theory, the threshold theorem, states that there exists a threshold error rate under which a quantum processor, even if faulty, is able to correctly run a quantum algorithm by using an efficient number of qubits and quantum gates [25]. The theorem guarantees that a quantum processor is feasible but only on the condition that the quantum error rate is kept low enough. Because of the aforementioned brittleness of the quantum coherence, this condition can be attained only by adopting quantum error correction (QEC) codes [25].

The unavoidable non-idealities in the actual implementation of quantum gates also prevent quantum gates from functioning ideally. Fidelity is the figure of merit that quantifies the difference between the output states generated by actual and ideal quantum gates [26]. The key point is that the QEC codes can be successfully applied only if quantum gate fidelities are higher than a given threshold [27]. A high enough quantum gate fidelity is therefore the prerequisite for achieving quantum fault tolerance.

The non-idealities in the electronic circuitry in an RFIC may limit the quantum gate fidelity [28,29]. For instance, the phase noise, affecting the microwave signal generated by the oscillator/phase locked loop in the RFIC, and the inaccuracies in the amplitude of the controlling microwave signal due to the output pre-drive amplifier in the RFIC can reduce the fidelity. The RFIC should be placed close to the qubits inside the cryostat chamber, whose thermal budget nevertheless limits the amount of power the RFIC is allowed to dissipate. Designing RFICs under power dissipation constraints may lead to device size, bias voltage, and low power circuit solutions that sacrifice ideal behavior for power [4,20]. For instance, power dissipation is traded for sensitivity to parametric fluctuations, the spurious free dynamic range (SFDR), and linearity.

Since quantum gate fidelity enables the application of the QEC codes, it is an important specification for electronics engineers designing the qubit RFIC controllers. Typical quantum gate fidelity requirements pose a significant challenge to the RFIC designers [10,30,31], who should therefore be aware of what quantum gate fidelity is, in order to properly account for it alongside other design specifications. In addition, being aware of quantum gate fidelity also facilitates discussion and information exchange between RFIC designers and physicists. Collaboration between these two professional figures is of paramount importance for successfully addressing the fabrication of quantum microprocessors.

Nevertheless, the literature typically addresses quantum gate fidelity by definition, without providing a rationalized explanation that aids understanding. Moreover, it employs advanced abstract mathematical formalism that does not help electronics engineers grasp the concept. This paper intends to contribute to overcoming these obstacles.

To achieve this, Section 2 of this paper introduces quantum gate fidelity by leveraging the concept of fidelity as found in information theory, which is generally familiar to electronics engineers. Moreover, Section 3 introduces an analogy between a quantum gate and a transmission channel, thus linking the input and output states of the quantum gate to, respectively, the transmitted and received signals on the channel. Section 4 reports a step-by-step, detailed mathematical proof of a relatively well-known formula for quantum gate fidelity [32]. This formula is particularly relevant for RFIC designers because it reduces the calculation of the fidelity to matrix analysis, a domain familiar to electronics engineers. Regrettably, in [32], as it often occurs in other papers on fidelity, see, for instance, refs. [33–35], the mathematics is often presented using an abstract formalism characteristic of theoretical physics. This makes it difficult for electronics engineers to interpret the

formulation of fidelity, thereby discouraging its use, despite fidelity being a relevant design specification. In contrast, the mathematical proof proposed in Section 4 adopts a more accessible mathematical formalism, aligning with the mathematical background of electronics engineers. It is the authors' opinion that addressing mathematical issues in this way helps to demystify concepts that may remain otherwise obscure. With the aim of further clarifying the relevance of the formula above for RFIC designers, Section 5 discusses brief case studies that exemplify how the RFIC non-idealities impact quantum gate fidelity, and Section 6 addresses the relationship between quantum gate fidelity and the energy efficiency of the quantum microprocessor. Section 7 discusses quantum gate fidelity in the more involved case of mixed states. Eventually, Section 8 closes this paper by summarizing the obtained results and drawing some conclusions.

2. Fidelity According to Shannon

The concept of fidelity is rooted in the communication theory conceived by Claude Shannon (1916–2001) in 1948 at Bell Laboratories [36]. Shannon introduced the term fidelity to indicate the degree of exactness in recovering, at the receiver side R_X of a transmission channel, the signal generated by a source at the transmitter side T_X. In particular, his historical paper introduces the probability $P(m_{IN}, m_{OUT})$, which represents, as follows, the likelihood that m_{OUT} and m_{IN} are, respectively, the input and output signals:

$$P(m_{IN}, m_{OUT}) = P(m_{IN})P(m_{OUT}|m_{IN}) \tag{1}$$

where $P(m_{IN})$ is the probability that the input message source generates the signal m_{IN} and $P(m_{OUT}|m_{IN})$ is the conditional probability that the received signal is m_{OUT} given that the sent message is m_{IN}. The conditional probability in Equation (1) implicitly attributes a stochastic nature to the transmission channel. Indeed, it introduces the fact that, for a given input signal, different output signals may be observed, each with its own conditional probability. All possible messages m_{IN} and m_{OUT} form the message space S_m. The probability $P(m_{IN}, m_{OUT})$ fully statistically describes the whole transmission system (message source plus transmission channel) in terms of the pairs of messages m_{IN} and m_{OUT}. If the probability $P(m_{IN}, m_{OUT})$ is known for the whole space S_m, the fidelity is also known in a qualitative sense. Nevertheless, if you desire a more operative and quantitative definition of fidelity, you need to introduce a function $F\{\cdot\}$ that yields a number from $P(m_{IN}, m_{OUT})$. Shannon interpreted this number as the distance between the ideally expected and the actually received output signals. He dubbed this distance fidelity because it quantifies the degree of exactness in receiving the transmitted message. In his paper, Shannon mathematically introduced fidelity as the weighted average distance calculated over the message space, where the probability $P(m_{IN}, m_{OUT})$ serves as the weighting factor [36]:

$$F\{P(m_{IN}, m_{OUT})\} = \sum_{S_m} P(m_{IN}, m_{OUT})\delta(m_{IN}, m_{OUT}) \tag{2}$$

where $\delta(m_{IN}, m_{OUT})$ quantifies, based on a given criterion, the distance between the received m_{OUT} and the transmitted m_{IN} signals. This makes sense because for an ideal transmission channel, the ideal received output signal $m_{OUT}^{I} = m_{IN}$, where the superscript "I" stands for ideal. The quantity $\delta(m_{IN}, m_{OUT})$ therefore measures the distance between the ideal and actual output messages. Since in Equations (1) and (2), m_{OUT} is the actual output signal, for reasons of unambiguousness, it is good practice to replace the symbol m_{OUT}

with m^R_{OUT} in these equations. With these representations, the substitution of Equation (1) into Equation (2) yields:

$$F\left\{P\left(m^I_{OUT}, m^R_{OUT}\right)\right\} = \sum_{S_m} P(m_{IN}) P\left(m^R_{OUT}\middle| m_{IN}\right) \delta\left(m^I_{OUT}, m^R_{OUT}\right) \tag{3}$$

where, in the mathematical expressions of the distance δ and fidelity F, it has been emphasized that $m^I_{OUT} = m_{IN}$. In this way, it is made plain that the distance δ and fidelity F address the difference between the ideal m^I_{OUT} and actual m^R_{OUT} output messages.

A deterministic (not stochastic) transmission channel implies $P\left(m^R_{OUT}\middle| m_{IN}\right) = 1$, reducing the mathematical expression of the fidelity to the following:

$$F\left\{P\left(m^I_{OUT}, m^R_{OUT}\right)\right\} = \sum_{S_m} P(m_{IN}) \delta\left(m^I_{OUT}, m^R_{OUT}\right) \tag{4}$$

It is worth noticing that, being deterministic, the channel does not imply an ideal channel. The distance δ in Equation (4) accounts for that. In particular, since $m^I_{OUT} = m_{IN}$, Equation (4) shows that different m_{IN} signals contribute differently to the fidelity.

In cases where the input source generates input messages with a uniform probability, the probability $P(m_{IN})$ is a constant, so you can factor it out from the summation:

$$F\left\{P\left(m^I_{OUT}, m^R_{OUT}\right)\right\} = P(m_{IN}) \sum_{S_m} \delta\left(m^I_{OUT}, m^R_{OUT}\right) \tag{5}$$

Apart from a constant, the fidelity can therefore be rewritten as follows:

$$F\left\{P\left(m^I_{OUT}, m^R_{OUT}\right)\right\} = \sum_{S_m} \delta\left(m^I_{OUT}, m^R_{OUT}\right) \tag{6}$$

If the space S_m is continuous instead of discrete, as assumed above, an integral replaces the summation:

$$F\left\{P\left(m^I_{OUT}, m^R_{OUT}\right)\right\} = \int_{S_m} \delta\left(m^I_{OUT}, m^R_{OUT}\right) dS_m \tag{7}$$

with dS_m being the infinitesimal volume in S_m. Equations (6) and (7) state that the fidelity is the average distance between m^I_{OUT} and m^R_{OUT} on the message space S_m.

It is worth concluding this section by emphasizing that Equations (6) and (7) embed two hypotheses: the transmission channel is deterministic, and all input signals are generated with the same probability.

3. The Fidelity of a Quantum Gate

Quantum gate fidelity, as well as the fidelity for transmitted and received signals in Section 2, quantifies the difference between ideal and actual quantum gates as the average distance between ideal and actual quantum output states. A fidelity equal to 100% means that the quantum gates behave ideally. In practice, it is useful to introduce the error rate of a quantum gate as the complement to 100% of the quantum fidelity [37], so that an ideal quantum gate exhibits an error rate equal to zero.

In quantum information theory, a quantum operation, such as a quantum gate, is an operator A [26,38]. Following the considerations in Section 2, this paper assimilates a real quantum gate to a real channel, as depicted in Figure 1. The output quantum state $|\psi^R_{OUT}\rangle = A\,|\psi_{IN}\rangle$ coincides with the ideal one $|\psi^I_{OUT}\rangle$ only if the operator is ideal, exactly as the output signal m_{OUT} is identical to the input signal m_{IN} only if the channel behaves ideally. If the effect of the quantum gate in Figure 1 on the input state $|\psi_{IN}\rangle$ does not

introduce phase decoherence, the output state $|\psi_{OUT}^{R}\rangle$ is a pure state as long as the input state is pure. Appendix A shortly reviews the definition of pure and mixed states, along with some further considerations.

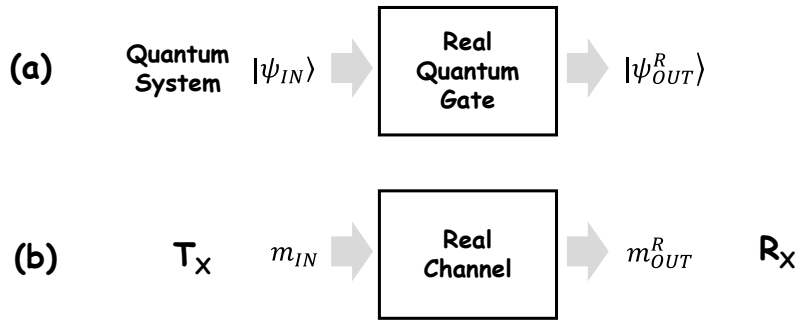

Figure 1. Analogy between the manipulation of a quantum state by a real quantum gate (**a**), and the transmission of a signal through a real channel (**b**).

As observed for a deterministic transmission channel, a coherent quantum gate does not imply that it behaves ideally. When both input and output states are pure, the distance $\delta(m_{OUT}^{I}, m_{OUT}^{R})$ is the state overlap probability $\delta(|\psi_{OUT}^{I}\rangle, |\psi_{OUT}^{R}\rangle) = |\langle\psi_{OUT}^{I}|\psi_{OUT}^{R}\rangle|^2$, which is the probability that the actual output state $|\psi_{OUT}^{R}\rangle$ coincides with the desired ideal $|\psi_{OUT}^{I}\rangle$ [38]. It is worth emphasizing here that, in quantum mechanics, the quantity $\langle\psi_{OUT}^{I}|\psi_{OUT}^{R}\rangle$ is dubbed the inner product, and it is a complex-valued scalar. By assuming that all input states are equally probable, the fidelity F of the quantum gate can be therefore introduced from Equation (7) as follows:

$$F = \int_{BS} \left|\left\langle \psi_{OUT}^{I} \middle| \psi_{OUT}^{R} \right\rangle\right|^2 dV \tag{8}$$

where dV is the infinitesimal volume of the Bloch sphere (BS), which is a geometrical figure useful for visualizing a quantum state [26,38]. For a n-level quantum state (qudit), the Bloch sphere is a hypersphere in a (2n−1)-dimensional space S^{2n-1} and it can be described as a nested Bloch sphere [39]. A qubit is a qudit for n = 2. In this case, the Bloch hypersphere reduces to the usual three-dimensional sphere, because 2n−1 = 3. It is worth pointing out that, as Equation (7) is an average value on the message space S_m, Equation (8) describes the fidelity F as the probability, averaged on the entire Bloch hypersphere, that $|\psi_{OUT}^{I}\rangle$ and $|\psi_{OUT}^{R}\rangle$ are identical.

If A_I and A_R are the ideal and actual forms, respectively, of the operator A, you can express $|\psi_{OUT}^{I}\rangle = A_I|\psi_{IN}\rangle$ and $|\psi_{OUT}^{R}\rangle = A_R|\psi_{IN}\rangle$. Thus:

$$F = \int_{BS} \left|\left\langle \psi_{IN} \middle| A_I^{\dagger} A_R \middle| \psi_{IN} \right\rangle\right|^2 dV \tag{9}$$

where $A_I^{\dagger}$ is the conjugate transpose (adjoint) of A_I. If the input state $|\psi_{IN}\rangle$ is a vector of an n-dimensional complex Hilbert space:

$$|\psi_{IN}\rangle = \sum_{i=1}^{n} \alpha_i |\psi_i\rangle \tag{10}$$

where $|\psi_i\rangle$ for i=1...n, is an orthonormal basis for the Hilbert space, Equation (9) can be reformulated as follows:

$$F = \int_{S^{2n-1}} \left|\left\langle \psi_{IN} \middle| A_I^{\dagger} A_R \middle| \psi_{IN} \right\rangle\right|^2 dV \tag{11}$$

In Equation (11), $|\psi_{IN}\rangle$ describes a qudit and the integral is calculated based on the Bloch hypersphere in the multi-dimensional space S^{2n-1}.

4. Quantum Gate Fidelity in Matrix Form

Calculating the fidelity from Equation (11) is not a trivial task, as it involves a multi-dimensional integral. The aim of this section is to formulate Equation (11) in a more practical matrix form, to make it easy to calculate the quantum fidelity once the operators A_I and A_R are provided in the matrix form. It is worth emphasizing that, once a basis for the Hilbert space is provided, an operator is mathematically represented by a matrix [40]; in this way, an operator enjoys all the properties of the matrix. In particular, the application of the Toeplitz decomposition [41] to the $A_{TOT} = A_I^{\dagger} A_R$ total operator makes it possible to decompose A_{TOT} into the sum of a Hermitian H and an anti-Hermitian A operator. Equation (11) can thus be rewritten as follows:

$$F = \int_{S^{2n-1}} |\langle \psi_{IN}|A_{TOT}|\psi_{IN}\rangle|^2 dV = \int_{S^{2n-1}} |\langle \psi_{IN}|H + A|\psi_{IN}\rangle|^2 dV \tag{12}$$

Because of linearity, Equation (12) can be reformulated as follows:

$$F = \int_{S^{2n-1}} |\langle \psi_{IN}|H|\psi_{IN}\rangle + \langle \psi_{IN}|A|\psi_{IN}\rangle|^2 dV \tag{13}$$

By assuming that the state $|\psi_{IN}\rangle$ is normalized, the quantities $\langle \psi_{IN}|H|\psi_{IN}\rangle$ and $\langle \psi_{IN}|A|\psi_{IN}\rangle$ are the expectation values of the operators H and A, respectively [42,43]. Since the expectation value of an operator is the average values of its eigenvalues [42,43], you can write:

$$\begin{aligned} \langle \psi_{IN}|H|\psi_{IN}\rangle &= \sum_i |\alpha_i|^2 h_i \\ \langle \psi_{IN}|A|\psi_{IN}\rangle &= \sum_i |\alpha_i|^2 a_i \end{aligned} \tag{14}$$

where α_i is the components of the state vector $|\psi_{IN}\rangle$ and h_i (a_i) are the eigenvalues of the operator H (A). By emphasizing that the eigenvalues of a Hermitian operator are real numbers while the eigenvalues of an anti-Hermitian operator are pure imaginary numbers [42], you can state that h_i are real numbers while a_i are imaginary numbers. In addition, since $|\alpha_i|^2$ are real numbers, you can conclude, from Equation (14), that $\langle \psi_{IN}|H|\psi_{IN}\rangle$ is real while $\langle \psi_{IN}|A|\psi_{IN}\rangle$ is purely imaginary. The argument of the integral in Equation (13) is therefore of the general form $|x + jy|^2$, with x and y real numbers. By emphasizing that $|x + jy|^2 = |x|^2 + |y|^2$, Equation (13) can be split into two contributions:

$$F = \int_{S^{2n-1}} |\langle \psi_{IN}|H|\psi_{IN}\rangle|^2 dV + \int_{S^{2n-1}} |\langle \psi_{IN}|A|\psi_{IN}\rangle|^2 dV \tag{15}$$

It is now also worth emphasizing that the Hermitian and anti-Hermitian operators are normal operators [44]. They therefore enjoy the spectral theorem from the matrix analysis [41], which states that every normal operator is unitarily similar to a diagonal operator, which is an operator represented by a diagonal matrix [44]. In particular, the matrix entries on the main diagonal are exactly the eigenvalues d_{Hi} for the diagonal operator D_H, which is similar to the operator H, and d_{Ai} for the diagonal operator D_A, which is similar to the operator A. Since similar operators exhibit the same eigenvalues, $h_i = d_{Hi}$ and $a_i = d_{Ai}$. Thus:

$$\begin{aligned} \langle \psi_{IN}|D_H|\psi_{IN}\rangle &= \sum_i |\alpha_i|^2 d_{Hi} = \sum_i |\alpha_i|^2 h_i \\ \langle \psi_{IN}|D_A|\psi_{IN}\rangle &= \sum_i |\alpha_i|^2 d_{Ai} = \sum_i |\alpha_i|^2 a_i \end{aligned} \tag{16}$$

Of course, with h_i (a_i) being real (imaginary) numbers, d_{Hi} (d_{Ai}) are also real (imaginary) numbers. The comparison of Equation (14) with Equation (16) leads to the following reformulation of Equation (15):

$$F = \int_{S^{2n-1}} |\langle \psi_{IN}|D_H|\psi_{IN}\rangle|^2 dV + \int_{S^{2n-1}} |\langle \psi_{IN}|D_A|\psi_{IN}\rangle|^2 dV \tag{17}$$

Since d_{Ai} is wholly imaginary, d_{Ai}/j is a real number and, since $|j| = 1$, Equation (17) can be reformulated by replacing D_A, whose entries are d_{Ai}, with D_A/j, whose entries are d_{Ai}/j:

$$F = \int_{S^{2n-1}} |\langle \psi_{IN}|D_H|\psi_{IN}\rangle|^2 dV + \int_{S^{2n-1}} |\langle \psi_{IN}|D_A/j|\psi_{IN}\rangle|^2 dV \tag{18}$$

In this way, the fidelity F has been expressed by means of the two real diagonal matrices D_H and D_A/j. For the sake of brevity, it therefore makes sense to address the following integral $\mathfrak{H}$:

$$\mathfrak{H} = \int_{S^{2n-1}} |\langle \psi_{IN}|D|\psi_{IN}\rangle|^2 dV \tag{19}$$

where D is a real diagonal matrix of real-valued eigenvalues d_i. The expectation value $\langle \psi_{IN}|D|\psi_{IN}\rangle$ is thus also real-valued, because of the usual expression:

$$\langle \psi_{IN}|D|\psi_{IN}\rangle = \sum_i |\alpha_i|^2 d_i \tag{20}$$

Since the squared module of a real number is the squared number $|\langle \psi_{IN}|D|\psi_{IN}\rangle|^2 = \langle \psi_{IN}|D|\psi_{IN}\rangle^2$, Equation (20) yields:

$$|\langle \psi_{IN}|D|\psi_{IN}\rangle|^2 = \left(\sum_i |\alpha_i|^2 d_i\right)^2 = \sum_i |\alpha_i|^4 d_i^2 + 2\sum_{i,j\neq i} |\alpha_i|^2 |\alpha_j|^2 d_i d_j \tag{21}$$

Equation (21) is the generalization to n terms of the Leibniz trinomial for n = 2 $(a+b+c)^2 = a^2+b^2+c^2+2ab+2ac+2bc$.

The substitution of Equation (21) into Equation (19) yields:

$$\mathfrak{H} = \int_{S^{2n-1}} \sum_i |\alpha_i|^4 d_i^2 dV + \int_{S^{2n-1}} 2\sum_{i,j\neq i} |\alpha_i|^2 |\alpha_j|^2 d_i d_j dV \tag{22}$$

from which:

$$\mathfrak{H} = \sum_i \left(\int_{S^{2n-1}} |\alpha_i|^4 dV\right) d_i^2 + \sum_i \left(\int_{S^{2n-1}} |\alpha_i|^2 |\alpha_j|^2 dV\right) 2 d_i d_j \tag{23}$$

The eigenvectors can be factored out from the integral because the integral is calculated on the (2n − 1)-dimensional Bloch hypersphere by varying the vector state $|\psi_{IN}\rangle$, i.e., by varying its components. Appendix B details the mathematical proof of the following pair of integrals:

$$\begin{array}{l} \int_{S^{2n-1}} |\alpha_i|^4 dV = \frac{2}{n(n+1)} \\ \int_{S^{2n-1}} |\alpha_i|^2 |\alpha_j|^2 dV = \frac{1}{n(n+1)} \end{array} \tag{24}$$

The substitution of Equation (24) into Equation (23) yields:

$$\mathfrak{H} = \frac{2}{n(n+1)} \sum_i d_i^2 + \frac{1}{n(n+1)} \sum_i 2 d_i d_j \tag{25}$$

By remarking that the trace $Tr\{D\}$ of the matrix D is also a real-valued number, you can write:

$$|Tr\{D\}|^2 = Tr^2\{D\} = \left(\sum_i d_i\right)^2 = \sum_i d_i^2 + 2\sum_{i,j\neq i} d_i d_j = Tr\left\{D^2\right\} + 2\sum_{i,j\neq i} d_i d_j \quad (26)$$

where it has been remarked that the first summation on the right-hand side of Equation (26) is the trace $Tr\left\{D^2\right\}$ of D^2.

Eventually, the substitution of Equation (26) into Equation (25) yields:

$$\mathfrak{H} = \frac{2}{n(n+1)}\sum_i d_i^2 + \frac{1}{n(n+1)}\left(|Tr\{D\}|^2 - Tr\left\{D^2\right\}\right) \quad (27)$$

Again, the summation in Equation (27) is $Tr\left\{D^2\right\}$, so that the Equation can be rearranged by factoring out $Tr\left\{D^2\right\}$:

$$\mathfrak{H} = Tr\left\{D^2\right\}\left[\frac{2}{n(n+1)} - \frac{1}{n(n+1)}\right] + \frac{1}{n(n+1)}|Tr\{D\}|^2 = \frac{Tr\left\{D^2\right\} + |Tr\{D\}|^2}{n(n+1)} \quad (28)$$

The application of Equation (28) to the real diagonal matrices D_H and D_A/j in Equation (18) leads to:

$$\begin{array}{rl} F & = \frac{Tr\left\{D_H^2\right\}+|Tr\{D_H\}|^2}{n(n+1)} + \frac{Tr\left\{(D_A/j)^2\right\}+|Tr\{D_A/j\}|^2}{n(n+1)} \\ & = \frac{Tr\left\{D_H^2\right\}+|Tr\{D_H\}|^2}{n(n+1)} + \frac{-Tr\left\{D_A^2\right\}+|Tr\{D_A\}|^2}{n(n+1)} \end{array} \quad (29)$$

Since D_H (D_A) is a diagonal matrix, whose entries are pure real (imaginary), $D_H = D_H^\dagger$ ($D_A = -D_A^\dagger$) and thus:

$$\begin{array}{l} D_H^2 = D_H D_H^\dagger \\ D_A^2 = -D_A D_A^\dagger \end{array} \quad (30)$$

Since H and D_H (D_A) are unitarily similar, by definition, D_H (D_A) is obtained from H (A) by means of the following similarity transformation:

$$\begin{array}{l} D_H = U_H^{-1} H U_H \\ D_A = U_A^{-1} A U_A \end{array} \quad (31)$$

where U_H (U_A) is the diagonalizing unitary matrix. The substitution of Equation (31) into Equation (30) yields:

$$\begin{array}{l} D_H^2 = U_H^{-1} H U_H \left(U_H^{-1} H U_H\right)^\dagger = U_H^{-1} H U_H \left[U_H^{-1}(H U_H)\right]^\dagger \\ D_A^2 = -U_A^{-1} A U_A \left(U_A^{-1} A U_A\right)^\dagger = -U_A^{-1} A U_A \left[U_A^{-1}(A U_A)\right]^\dagger \end{array} \quad (32)$$

Since, for a unitary matrix, $U^{-1} = U^\dagger$, and, for a couple of matrices A and B, $(AB)^\dagger = B^\dagger A^\dagger$, Equation (32) can be reformulated as follows:

$$\begin{array}{l} D_H^2 = U_H^{-1} H U_H \, (H U_H)^\dagger U_H^{-1\dagger} = U_H^{-1} H U_H U_H^\dagger H^\dagger U_H = U_H^{-1} H H^\dagger U_H \\ D_A^2 = -U_A^{-1} A U_A \, (A U_A)^\dagger U_A^{-1\dagger} = -U_A^{-1} A U_A U_A^\dagger A^\dagger U_A = -U_A^{-1} A A^\dagger U_A \end{array} \quad (33)$$

By emphasizing that, for a pair of matrices A and B, $Tr\{AB\} = Tr\{BA\}$, from Equation (33), you get:

$$\begin{aligned} Tr\{D_H^2\} &= Tr\left\{\left(U_H^{-1}H\right)(H^\dagger U_H)\right\} = Tr\left\{(H^\dagger U_H)\left(U_H^{-1}H\right)\right\} = Tr\{H^\dagger H\} \\ Tr\{D_A^2\} &= -Tr\left\{\left(U_A^{-1}A\right)(A^\dagger U_A)\right\} - Tr\left\{(A^\dagger U_A)\left(U_A^{-1}A\right)\right\} = -Tr\{A^\dagger A\} \end{aligned} \tag{34}$$

and from Equation (31):

$$\begin{aligned} Tr\{D_H\} &= Tr\left\{\left(U_H^{-1}H\right)U_H\right\} = Tr\left\{U_H\left(U_H^{-1}H\right)\right\} = Tr\left\{U_H U_H^{-1}H\right\} = Tr\{H\} \\ Tr\{D_A\} &= Tr\{A\} \end{aligned} \tag{35}$$

The substitution of Equations (34) and (35) into Equation (29) yields:

$$F = \frac{Tr\{H^\dagger H\} + Tr\{A^\dagger A\} + |Tr\{H\}|^2 + |Tr\{A\}|^2}{n(n+1)} \tag{36}$$

By emphasizing that $A_{TOT} = H + A$, you can write:

$$Tr\left\{A_{TOT}A_{TOT}^\dagger\right\} = Tr\left\{(H+A)(H+A)^\dagger\right\} = Tr\{(H+A)(H-A)\} \tag{37}$$

where it has been emphasized that, by definition, $H^\dagger = H$ and $A^\dagger = -A$. Due to the above-emphasized property $Tr\{AB\} = Tr\{BA\}$, it holds that $Tr\{HA\} = Tr\{AH\}$. Thus, Equation (37) can be shortened as follows:

$$Tr\left\{A_{TOT}A_{TOT}^\dagger\right\} = Tr\{HH\} - Tr\{HA\} + Tr\{AH\} - Tr\{AA\} = Tr\left\{HH^\dagger\right\} + Tr\left\{AA^\dagger\right\} \tag{38}$$

From Equation (31), you can observe that similar matrices own the same trace:

$$\begin{aligned} Tr\{D_H\} &= Tr\left\{\left(U_H^{-1}H\right)U_H\right\} = Tr\left\{U_H U_H^{-1}H\right\} = Tr\{H\} \\ Tr\{D_A\} &= Tr\{A\} \end{aligned} \tag{39}$$

Equation (39) shows that the trace of H (A) is real (imaginary), because the entries of D_H (D_A) are real (imaginary). Consequently, you can write:

$$|Tr\{A_{TOT}\}|^2 = |Tr\{H+A\}|^2 = |Tr\{H\} + Tr\{A\}|^2 = |Tr\{H\}|^2 + |Tr\{A\}|^2 \tag{40}$$

The substitution of Equations (38) and (40) into Equation (36) yields:

$$F = \frac{Tr\left\{A_{TOT}A_{TOT}^\dagger\right\} + |Tr\{A_{TOT}\}|^2}{n(n+1)} \tag{41}$$

It is now worth emphasizing that the operator describing a quantum gate is unitary and thus represented by a unitary matrix. Since A_I and A_R are unitary operators, being the operators of a quantum gate, the operator A_{TOT}, which is their product, is also unitary and thus $A_{TOT}^{-1} = A_{TOT}^\dagger$. Equation (41) therefore takes the following form:

$$F = \frac{Tr\{I\} + |Tr\{A_{TOT}\}|^2}{n(n+1)} = \frac{n + \left|Tr\left\{A_I^\dagger A_R\right\}\right|^2}{n(n+1)} \tag{42}$$

Equation (42) provides the mathematical expression for the fidelity of a quantum gate exploiting an n-level quantum system, as it has been calculated for a general qudit. In the case of a one-qubit gate (e.g., X Pauli gate), n = 2, since there are two energy levels, while for a two-qubit gate (e.g., CNOT gate), n = 4 because there are four energy levels [22].

5. Brief Case Studies

To better grasp the relevance of Equation (42) as an RFIC designer, let us consider the brief case studies of the one-qubit Pauli X and two-qubit CNOT quantum gates implemented in the spin of electrons confined in quantum wells [22]. The quantum gate is implemented by irradiating the qubit, via a micro-antenna, with a microwave pulse at the resonance Larmor frequency and for a suitable time duration Δt; this microwave irradiation induces the following rotation angle θ of the state vector:

$$\boldsymbol{\theta = \frac{g\mu_B}{2\hbar} B_1 \Delta t} \tag{43}$$

where $\boldsymbol{g}$ is the electron spin g-factor, $\boldsymbol{\mu_B}$ is the Bohr magneton, $\hbar$ is the reduced Planck constant, and $\boldsymbol{B_1}$ is the magnitude of the magnetic component of the microwave electromagnetic pulse applied to the qubit. The magnitude $\boldsymbol{B_1}$ depends on the amplitude of the microwave signal $\boldsymbol{s_{RF}}$, generated by the RFIC, which excites the micro-antenna used to irradiate the qubit.

5.1. Pauli X Quantum Gate

The ideal matrix $\boldsymbol{A_{XI}}$ of the Pauli X quantum gate operator is obtained from the matrix $\boldsymbol{A_{RX}}$ of the $\boldsymbol{R_X}$ operator [22]:

$$\boldsymbol{A_{RX} = \begin{bmatrix} cos\frac{\theta}{2} & -jsin\frac{\theta}{2} \\ -jsin\frac{\theta}{2} & cos\frac{\theta}{2} \end{bmatrix}} \tag{44}$$

by forcing the rotation angle of the qubit state vector $\boldsymbol{\theta = \pi}$ and by factorizing and neglecting the global phase term $\boldsymbol{-j}$:

$$\boldsymbol{A_{XI} = \begin{bmatrix} 0 & 1 \\ 1 & 0 \end{bmatrix}} \tag{45}$$

Let us suppose that the actual rotation angle is affected by an error $\boldsymbol{\varepsilon}$, so that $\boldsymbol{\theta = \pi + \varepsilon}$, because the electronics circuitry, designed to control the qubit, causes errors in the amplitude of $\boldsymbol{s_{RF}}$ and/or in the duration $\boldsymbol{\Delta t}$. From Equation (44), the actual matrix $\boldsymbol{A_{XR}}$ of the Pauli X quantum gate operator is:

$$\boldsymbol{A_{XR} = \begin{bmatrix} cos\left(\frac{\pi}{2}+\frac{\varepsilon}{2}\right) & -jsin\left(\frac{\pi}{2}+\frac{\varepsilon}{2}\right) \\ -jsin\left(\frac{\pi}{2}+\frac{\varepsilon}{2}\right) & cos\left(\frac{\pi}{2}+\frac{\varepsilon}{2}\right) \end{bmatrix} = -\begin{bmatrix} sin\left(\frac{\varepsilon}{2}\right) & jcos\left(\frac{\varepsilon}{2}\right) \\ jcos\left(\frac{\varepsilon}{2}\right) & sin\left(\frac{\varepsilon}{2}\right) \end{bmatrix}} \tag{46}$$

Since the entries of the matrix $\boldsymbol{A_{XI}}$ are real values, $\boldsymbol{A_{XI} = A_{XI}^{\dagger}}$, and thus from Equations (45) and (46), you obtain:

$$\boldsymbol{A_{XI}^{\dagger} A_{XR} = -\begin{bmatrix} 0 & 1 \\ 1 & 0 \end{bmatrix} \begin{bmatrix} sin\left(\frac{\varepsilon}{2}\right) & jcos\left(\frac{\varepsilon}{2}\right) \\ jcos\left(\frac{\varepsilon}{2}\right) & sin\left(\frac{\varepsilon}{2}\right) \end{bmatrix} = -\begin{bmatrix} jcos\left(\frac{\varepsilon}{2}\right) & sin\left(\frac{\varepsilon}{2}\right) \\ sin\left(\frac{\varepsilon}{2}\right) & jcos\left(\frac{\varepsilon}{2}\right) \end{bmatrix}} \tag{47}$$

from which:

$$\boldsymbol{\left| Tr\left\{ A_{XI}^{\dagger} A_{XR} \right\} \right|^2 = \left| -2jcos\left(\frac{\varepsilon}{2}\right) \right|^2 = 4cos^2\left(\frac{\varepsilon}{2}\right)} \tag{48}$$

The substitution of Equation (48) into Equation (42) yields:

$$\boldsymbol{F = \frac{2 + 4cos^2\left(\frac{\varepsilon}{2}\right)}{2(2+1)} = \frac{1 + 2cos^2\left(\frac{\varepsilon}{2}\right)}{3}} \tag{49}$$

where it has been emphasized that n = 2 for a one-qubit quantum gate. As expected, Equation (49) yields $\boldsymbol{F = 1}$ when $\boldsymbol{\varepsilon = 0}$.

5.2. CNOT Quantum Gate

As for the CNOT quantum gate operator, its ideal matrix A_{CNOTI} is obtained from the matrix $A_{\omega R1,I}$ [22]:

$$A_{\omega R1,I} = \begin{bmatrix} -j & 0 & 0 & 0 \\ 0 & -j & 0 & 0 \\ 0 & 0 & cos\left(\frac{\theta}{2}\right) & -jsin\left(\frac{\theta}{2}\right) \\ 0 & 0 & -jsin\left(\frac{\theta}{2}\right) & cos\left(\frac{\theta}{2}\right) \end{bmatrix} \quad (50)$$

by forcing the rotation angle of the qubit state vector $\theta = \pi$ and by factorizing and neglecting the global phase term $-j$:

$$A_{CNOTI} = \begin{bmatrix} 1 & 0 & 0 & 0 \\ 0 & 1 & 0 & 0 \\ 0 & 0 & 0 & 1 \\ 0 & 0 & 1 & 0 \end{bmatrix} \quad (51)$$

As in the previous case, let the actual rotation angle be affected by an error ε, so that $\theta = \pi + \varepsilon$. Equation (50) yields the actual matrix A_{CNOTR} of the CNOT quantum gate operator:

$$\begin{aligned} A_{CNOTR} &= \begin{bmatrix} -j & 0 & 0 & 0 \\ 0 & -j & 0 & 0 \\ 0 & 0 & cos\left(\frac{\pi}{2}+\frac{\varepsilon}{2}\right) & -jsin\left(\frac{\pi}{2}+\frac{\varepsilon}{2}\right) \\ 0 & 0 & -jsin\left(\frac{\pi}{2}+\frac{\varepsilon}{2}\right) & cos\left(\frac{\pi}{2}+\frac{\varepsilon}{2}\right) \end{bmatrix} \\ &= \begin{bmatrix} -j & 0 & 0 & 0 \\ 0 & -j & 0 & 0 \\ 0 & 0 & -sin\left(\frac{\varepsilon}{2}\right) & -jcos\left(\frac{\theta}{2}\right) \\ 0 & 0 & -jcos\left(\frac{\theta}{2}\right) & -sin\left(\frac{\varepsilon}{2}\right) \end{bmatrix} = -\begin{bmatrix} j & 0 & 0 & 0 \\ 0 & j & 0 & 0 \\ 0 & 0 & sin\left(\frac{\varepsilon}{2}\right) & jcos\left(\frac{\theta}{2}\right) \\ 0 & 0 & jcos\left(\frac{\theta}{2}\right) & sin\left(\frac{\varepsilon}{2}\right) \end{bmatrix} \end{aligned} \quad (52)$$

Since the entries of the matrix A_{CNOTI} are real values, $A_{CNOTI} = A^{\dagger}_{CNOTI}$. Thus, from Equations (51) and (52), you obtain:

$$\begin{aligned} A^{\dagger}_{CNOTI}A_{CNOTR} &= -\begin{bmatrix} 1 & 0 & 0 & 0 \\ 0 & 1 & 0 & 0 \\ 0 & 0 & 0 & 1 \\ 0 & 0 & 1 & 0 \end{bmatrix}\begin{bmatrix} j & 0 & 0 & 0 \\ 0 & j & 0 & 0 \\ 0 & 0 & sin\left(\frac{\varepsilon}{2}\right) & jcos\left(\frac{\theta}{2}\right) \\ 0 & 0 & jcos\left(\frac{\theta}{2}\right) & sin\left(\frac{\varepsilon}{2}\right) \end{bmatrix} = \\ &= -\begin{bmatrix} j & 0 & 0 & 0 \\ 0 & j & 0 & 0 \\ 0 & 0 & jcos\left(\frac{\varepsilon}{2}\right) & sin\left(\frac{\theta}{2}\right) \\ 0 & 0 & sin\left(\frac{\theta}{2}\right) & jcos\left(\frac{\varepsilon}{2}\right) \end{bmatrix} \end{aligned} \quad (53)$$

from which:

$$\left|Tr\left\{A^{\dagger}_{CNOTI}A_{CNOTR}\right\}\right|^2 = \left|-2j\left[1+cos\left(\frac{\varepsilon}{2}\right)\right]\right|^2 = 4\left[1+cos\left(\frac{\varepsilon}{2}\right)\right]^2 \quad (54)$$

The substitution of Equation (54) into Equation (42) yields:

$$F = \frac{4+4\left[1+cos\left(\frac{\varepsilon}{2}\right)\right]^2}{4(4+1)} = \frac{1+\left[1+cos\left(\frac{\varepsilon}{2}\right)\right]^2}{5} \quad (55)$$

where it has been emphasized that n = 4 for a two-qubit quantum gate. As expected, Equation (55) yields $F = 1$ when $\varepsilon = 0$.

5.3. Entanglement Fidelity

Finally, it is worth noting that the authors in [45] expressed the fidelity in Equation (42) in terms of the entanglement fidelity F_e:

$$\boldsymbol{F = \frac{nF_e + 1}{n + 1}} \tag{56}$$

where F_e quantifies the exactness in teleporting information coded in a quantum state over a quantum transmission channel formed by entangled states (e.g., Bell states). Equation (56) further reinforces the analogy proposed in Figure 1 between a quantum gate and a transmission channel. The substitution of Equation (42) into Equation (56) yields:

$$\boldsymbol{F_e = \frac{\left|Tr\left\{A_I^{\dagger} A_R\right\}\right|^2}{n^2}} \tag{57}$$

which is the mathematical expression used in [28] to investigate the impact of the non-ideal behavior of the electronics on quantum fidelity. In the above case studies with the Pauli X and CNOT quantum gates, the substitution of Equation (48) into Equation (57) yields the entanglement fidelity $F_{e,X}$ for the Pauli X quantum gate:

$$\boldsymbol{F_{e,X} = \frac{4cos^2\left(\frac{\varepsilon}{2}\right)}{2^2} = cos^2\left(\frac{\varepsilon}{2}\right) = 1 - sin^2\left(\frac{\varepsilon}{2}\right)} \tag{58}$$

and the subsititution of Equation (54) into Equation (57) yields the entanglement fidelity $F_{e,CNOT}$ for the CNOT quantum gate:

$$\boldsymbol{F_{e,CNOT} = \frac{4\left[1+cos\left(\frac{\varepsilon}{2}\right)\right]^2}{4^2} = \frac{2-sin^2\left(\frac{\varepsilon}{2}\right)+2cos\left(\frac{\varepsilon}{2}\right)}{4} = \frac{1-\frac{1}{2}sin^2\left(\frac{\varepsilon}{2}\right)+cos\left(\frac{\varepsilon}{2}\right)}{2}} \tag{59}$$

For small values of ε, $sin(\varepsilon/2)$ can be approximated with $\varepsilon/2$ and $cos(\varepsilon/2)$ with **1**, so that, from Equations (58) and (59), respectively, you obtain:

$$\boldsymbol{F_{e,X} \cong 1 - \left(\frac{\varepsilon}{2}\right)^2 = 1 - \frac{\varepsilon^2}{4}} \tag{60}$$

$$\boldsymbol{F_{e,CNOT} \cong \frac{1 - \frac{1}{2}\left(\frac{\varepsilon}{2}\right)^2 + 1}{2} = 1 - \frac{\varepsilon^2}{16}} \tag{61}$$

Equation (60) agrees with the mathematical form claimed in [24,28] for one-qubit quantum gates facing phase errors in the controlling microwave signal.

5.4. N-Qubit Quantum Gate

Equations (60) and (61) suggest that the entanglement fidelity $F_{e,NQUBIT}$ of an n-qubit quantum gate can be approximated as follows for small values of ε:

$$\boldsymbol{F_{e,NQUBIT} \cong 1 - \left(\frac{\varepsilon}{n}\right)^2} \tag{62}$$

The substitution of Equation (57) into Equation (62) yields:

$$\boldsymbol{\frac{\left|Tr\left\{A_I^{\dagger} A_R\right\}\right|^2}{n^2} = 1 - \left(\frac{\varepsilon}{n}\right)^2} \tag{63}$$

and thus:

$$\left|Tr\left\{A_I^{\dagger}A_R\right\}\right|^2 = n^2 - \varepsilon^2 \tag{64}$$

By adding n on both sides, you obtain:

$$\left|Tr\left\{A_I^{\dagger}A_R\right\}\right|^2 + n = n + n^2 - \varepsilon^2 \tag{65}$$

from which:

$$\frac{\left|Tr\left\{A_I^{\dagger}A_R\right\}\right|^2 + n}{n + n^2} = 1 - \frac{\varepsilon^2}{n + n^2} \tag{66}$$

By referring to Equation (42), Equation (66) can be written in a shorter form:

$$F = 1 - \frac{\varepsilon^2}{n + n^2} \tag{67}$$

from which:

$$\varepsilon = \sqrt{n(n+1)(1-F)} \tag{68}$$

Equation (68) is identical to the mathematical expression of the upper bound error claimed in [24] for an n-qubit quantum gate. It should be pointed out that the authors in [24] propose the Pauli distance as tool for a more accurate investigation of quantum gates.

For the sake of convenience, Table 1 summarizes the main obtained mathematical expressions for fidelity and entanglement fidelity.

Table 1. Mathematical expressions for fidelity and entanglement fidelity.

Quantum Gate	F	F_e	$F_e(\varepsilon \ll 1)$
One-qubit (Pauli X)	$\frac{1+2cos^2\left(\frac{\varepsilon}{2}\right)}{3}$	$1 - sin^2\left(\frac{\varepsilon}{2}\right)$	$1 - \frac{\varepsilon^2}{4}$
Two-qubit (CNOT)	$\frac{1+\left[1+cos\left(\frac{\varepsilon}{2}\right)\right]^2}{5}$	$\frac{1-\frac{1}{2}sin^2\left(\frac{\varepsilon}{2}\right)+cos\left(\frac{\varepsilon}{2}\right)}{2}$	$1 - \frac{\varepsilon^2}{16}$
N-qubit			$1 - \left(\frac{\varepsilon}{n}\right)^2$

Table 2 reports some experimental values of quantum fidelity for one-qubit and two-qubit quantum gates. It shows that achieving higher fidelities is simpler for one-qubit than for two-qubit quantum gates. On the other hand, Equation (67) implies that, for a given error, the fidelity increases with increasing n. This comparison suggests that actual quantum gates also suffer from environmental decoherence [25]. Equation (42), of which Equation (67) was demonstrated to be a consequence, can indeed account for coherent sources of error only, as it holds for pure states [25].

Table 2. Experimental quantum fidelity values for one- and two-qubit quantum gates.

Number of Qubits	Qubit Technology	Fidelity [%]	Reference
1	Superconducting	99.9	[46]
1	Superconducting	99.8	[47]
1	Superconducting	>99.9	[48]
1	Electron Spin	99.9	[49]
2	Superconducting	99.4	[47]
2	Superconducting	99.4	[46]
2	Trapped ions	99.3	[47]
2	Neutral atom	99.5	[37]

6. Energy Efficiency

As outlined in Section 1, in order to address problems of practical utility, quantum microprocessors need to protect the qubits against errors by adopting QEC codes. Nevertheless, these codes require fidelity that is better than a threshold value $F_{threshold}$ [37,50]. A QEC code implies merging N_{qubit} physical qubits into one logic qubit to achieve a desired logic error rate ε_{logic}, which decreases with increasing N_{qubit} [51]:

$$\varepsilon_{logic} = K_1 \left(\sqrt{\frac{1-F}{1-F_{threshold}}} \right)^{\frac{1}{2}\left(\sqrt{\frac{N_{qubit}+1}{2}}+1\right)} \tag{69}$$

with K_1 being a suitable constant. By emphasizing the definition of the error rate of a quantum gate given in Section 3, Equation (69) can be reformulated as follows:

$$\varepsilon_{logic} = K_1 \left(\sqrt{\frac{1-F}{\varepsilon_{threshold}}} \right)^{\frac{1}{2}\left(\sqrt{\frac{N_{qubit}+1}{2}}+1\right)} \tag{70}$$

where $\varepsilon_{threshold}$ is the error rate threshold required by the QEC code. From Equation (70), you can obtain:

$$N_{qubit} = 2\left[1 - 2\frac{log(\varepsilon_{logic}) - log(K_1)}{log\left(\frac{1-F}{\varepsilon_{threshold}}\right)}\right]^2 - 1 \cong 8\left[\frac{log(\varepsilon_{logic})}{log\left(\frac{1-F}{\varepsilon_{threshold}}\right)}\right]^2 \tag{71}$$

where the approximation is based on ε_{logic} being very small, in the order of 10^{-10} [51]. By defining P_{qubit} the power dissipated to control each physical qubit, Equation (71) provides the total dissipated power $P_{logical}$ for the logical qubit:

$$P_{logical} = P_{qubit}\left[\frac{log(\varepsilon_{logic})}{log\left(\frac{1-F}{\varepsilon_{threshold}}\right)}\right]^2 \tag{72}$$

where P_{qubit} depends on the adopted qubit-driving method [52]. The power $P_{logical}$ appears, magnified by the ratio between the room T_{room} and the qubit cryogenic T_{qubit} temperatures, in the power dissipated by the cryostat P_{cryo} [53]:

$$P_{cryo} = \frac{T_{room}}{T_{qubit}} P_{qubit}\left[\frac{log(\varepsilon_{logic})}{log\left(\frac{1-F}{\varepsilon_{threshold}}\right)}\right]^2 \tag{73}$$

Equation (73) demonstrates the importance of achieving a quantum gate fidelity that is as high as possible, as this makes the ratio $(1-F)/\varepsilon_{threshold}$ lower and reduces, in this way, P_{cryo}. Equation (73) also shows that hot qubits may help in reducing P_{QCPU}, because they reduce the temperature ratio T_{room}/T_{qubit}. Interestingly, one- and two-qubit quantum gates encoded in semiconductor electron spins operating above 1 K have been recently demonstrated to produce fidelity, respectively, of 99.6% and 98.9% [54].

7. Mixed States

Equation (42) has been proven under the assumptions that the input state is pure and uniformly distributed and that quantum gates do not introduce phase decoherence, ensuring that the output state is also pure. In practice, the uniform distribution of the input states may not be considered a serious limitation, because the characterization of a quantum

gate is typically intended to explore how the quantum gate behaves for all possible input states, as it occurs in the case of the quantum process tomography [55]. Several papers on average fidelity indeed assume a uniform distribution, such as, for instance, [34,56]. On the other hand, the case of mixed states is more involved and it deserves a more comprehensive discussion for the sake of comparison with the literature.

In cases where the input state $|\psi_{IN}\rangle$ of the density matrix is pure and the output state is mixed ρ_{OUT}, Wilde introduces the expected fidelity as an average distance $\langle\delta\rangle$ between pure states [38]:

$$\langle\delta\rangle = \sum_X p_X |\langle\psi_{IN}|\psi_X\rangle|^2 \tag{74}$$

where p_X is the probability used to describe the mixed state as a mixture of pure states in terms of a linear combination of the density matrix of pure states $|\psi_X\rangle$ (see Appendix A):

$$\rho_{OUT} = \sum_X p_X |\psi_X\rangle\langle\psi_X| \tag{75}$$

Since, as observed in Appendix A, a pure state is an ensemble of identical pure states, in cases where the output state is pure, Equation (75) reduces to $|\langle\psi_{IN}|\psi_{OUT}\rangle|^2$, being $|\psi_X\rangle = |\psi_{OUT}\rangle$ and $\sum_X p_X = 1$ for the probability normalization.

Wilde shows that a short algebraic manipulation leads to the following compact mathematical expression of Equation (75):

$$\langle\delta\rangle = \langle\psi_{IN}|\rho_{OUT}|\psi_{IN}\rangle \tag{76}$$

Equivalently, Equation (76) can be expressed by means of the trace Tr [57]:

$$\langle\delta\rangle = Tr\{|\psi_{IN}\rangle\langle\psi_{IN}|\rho_{OUT}\} = Tr\{\rho_{IN}\rho_{OUT}\} \tag{77}$$

Nielsen reports, as a root fidelity, a mathematical expression very close to Equation (76) [26]:

$$F = \sqrt{\langle\psi_{IN}|\rho_{OUT}|\psi_{IN}\rangle} \tag{78}$$

In the more involved case where, in addition to the output state, the input state is also mixed, Wilde invokes Uhlmann's fidelity [38], which, after [58] and [59], is defined as the maximum probability that the purifications of the two mixed states are coincident. Appendix A reports short notes about the concept of purification. Uhlmann's theorem allows the following compact mathematical expression for the fidelity [38]:

$$F = \|\sqrt{\rho_{IN}}\sqrt{\rho_{OUT}}\|_1 \tag{79}$$

where $\|\cdot\|_1$ is the Schatten 1-norm, defined as $Tr\left\{\sqrt{M^\dagger M}\right\}$ for a given operator M. Note that $\sqrt{\rho_{IN}}\sqrt{\rho_{OUT}}$ is indeed an operator, with the density matrix ρ_{IN} and ρ_{OUT} being operators. Moving from Equation (79), Wilde reports that it is possible to write Uhlmann's fidelity in the following trace form:

$$F = \left\{Tr\sqrt{\sqrt{\rho_{IN}}\rho_{OUT}\sqrt{\rho_{IN}}}\right\}^2 \tag{80}$$

Equation (80) reduces to Equation (76) when the input state is pure, because, for a pure state, it holds that $\rho^2 = \rho$ and $Tr\{\rho^2\} = 1$ [43]. The property $\rho^2 = \rho$ indeed allows for writing:

$$F = \{Tr\sqrt{\rho_{IN}\rho_{OUT}\rho_{IN}}\}^2 = \left\{Tr\sqrt{|\psi_{IN}\rangle\langle\psi_{IN}|\rho_{OUT}|\psi_{IN}\rangle\langle\psi_{IN}|}\right\}^2 \quad (81)$$

and since $\langle\psi_{IN}|\rho_{OUT}|\psi_{IN}\rangle$ is scalar, being an expectation value [43], Equation (81) can be rearranged as follows:

$$F = \left\{\sqrt{\langle\psi_{IN}|\rho_{OUT}|\psi_{IN}\rangle}Tr\sqrt{|\psi_{IN}\rangle\langle\psi_{IN}|}\right\}^2 = \langle\psi_{IN}|\rho_{OUT}|\psi_{IN}\rangle Tr^2\{\sqrt{\rho_{IN}}\} \quad (82)$$

Having emphasized that $Tr\{cM\} = cTr\{M\}$ for a given scalar c and operator M, invoking again the properties $\rho^2 = \rho$ and $Tr\{\rho^2\} = 1$ yields:

$$F = \langle\psi_{IN}|\rho_{OUT}|\psi_{IN}\rangle Tr^2\{\rho_{IN}\} = \langle\psi_{IN}|\rho_{OUT}|\psi_{IN}\rangle \quad (83)$$

which is equal to Equation (76). Equation (80) reduces to the distance $|\langle\psi_{IN}|\psi_{OUT}\rangle|^2$, used in Equation (8), when both the input and output states are pure. Having indeed proved that an input pure state leads from Equation (80) to Equation (76), it is just enough to state that Equation (76) is equivalent to Equation (74) and that the pure output state reduces Equation (74) to $|\langle\psi_{IN}|\psi_{OUT}\rangle|^2$, because $\sum_X p_X = 1$.

8. Conclusions

This paper provided a rationalization of the concept of quantum gate fidelity, starting from Shannon's fidelity and drawing an analogy between a quantum gate and a transmission channel. This approach introduces quantum gate fidelity to electronics engineers in a more accessible manner, leveraging their general background. Bringing quantum fidelity back to information theory concepts facilitates understanding its integral form in Equation (11). In contrast, other authors, such as in [32], introduce this integral form abstractly and associate it with fidelity without any justification.

This paper also proposed a step-by-step mathematical proof of Equation (42) using mathematical tools familiar to electronics engineers. Apart from some fundamentals of quantum mechanics and matrix analysis, for which reference textbooks [40–44] are suggested if needed, the proof primarily requires algebraic steps and hyperspace integrations (see Appendices B and C). Though longer than the one in [32], this proposed proof is significant, because Equation (42) is of relevance for RFIC designers. It indeed simplifies the quantum gate fidelity calculation from the abstract multi-dimensional integral in Equation (11) to the product between the matrices A_I and A_R, describing, respectively, the wanted ideal and actual behavior of the quantum gate. In particular, the proof begins by applying the Toeplitz decomposition, focusing on the single integral form in Equation (19), from which Equation (28) follows. In contrast, in [32], the Toeplitz decomposition appears only in a later phase, and multi-dimensional integrals are just stated. A mathematical expression close to Equation (28) is reported in [32], relying on particularly simple matrices and abstract formulas, but lacking proof or useful references.

To further clarify the use of Equation (42), Section 5 addressed case studies of Pauli X and CNOT quantum gates encoded in an electron spin, specifically analyzing the impact of phase error on fidelity. The implications of these results are then discussed in the light of entanglement fidelity and the error upper bound, reinforcing the central role of Equation (42).

The main implications of the results above are a facilitated understanding of quantum gate fidelity to electronics engineers and improved collaboration between engineers and physicists, which is important for the practice of applied research.

Section 6 also contributed to reinforcing the engineering relevance of Equation (42) by elucidating its impact on the energy efficiency of a quantum microprocessor.

Even if the experimental investigation of fidelity is not the subject of this paper, for the sake of completeness, it is worth closing these conclusions by remarking that the experimental verification of Equation (42) needs independent measurements of the fidelity and the actual matrix A_R of the quantum gate operator. For this purpose, several experimental techniques, each with its own advantages and downsides, can be adopted, such as the randomized benchmarking (RB) protocol [54], quantum process tomography (QPT) [26], or gate set tomography (GST) [49]. In this case, the fidelity is a process fidelity, calculated as the trace of the product matrix between the ideal process matrix and the Hermitian and unitary matrix that best fits the tomographic experimental data [60].

The experimental characterization of quantum gate fidelity is an important activity because it allows us to optimize microwave pulse parameters, such as shape, amplitude, and rise/fall times, for the best possible fidelity [49]. With this perspective, artificial intelligence (AI), when applied to experimental techniques for the characterization of quantum gate fidelity, may be a useful tool for optimizing the microwave control of the qubits [61,62].

QEC codes, briefly cited in Section 6, and AI applied to experimental characterization can therefore be considered promising strategies to improve the fidelity of quantum gates in the presence of practical limitations imposed by thermal noise and the accuracy of electronics circuitry.

Author Contributions: Conceptualization, methodology, writing—original draft preparation, visualization, supervision, M.B.; formal analysis, investigation, writing—review and editing, M.B. and A.B. All authors have read and agreed to the published version of the manuscript.

Funding: This research has been partially funded by the project: Addressing molecular and donorSpins with MIcrowave puLsEs through Superconducting circuits for Quantum Information Processing (SMILE-SQUIP); project code: PNRR-BAC E93C24001030001. European Community (NextGenerationEU).

Institutional Review Board Statement: Not applicable.

Informed Consent Statement: Not applicable.

Data Availability Statement: Data is contained within the article.

Conflicts of Interest: The authors declare no conflicts of interest.

Abbreviations

The following abbreviations are used in this manuscript:

Qubit	Quantum bit
BS	Bloch Sphere
RFIC	Radio Frequency Integrated Circuit
SFDR	Spurious Free Dynamic Range
QEC	Quantum Error Correction
AI	Artificial Intelligence
RB	Randomized Benchmarking
QPT	Quantum Process Tomography
GST	Gate Set Tomography

Appendix A

In quantum mechanics, a quantum state is pure when it provides a fully informative description of a quantum system. This implies that the quantum system is closed and

isolated from its environment, so that Schrödinger's Equation is an adequate tool for describing the dynamics of the system [63]. Nevertheless, when addressing open quantum systems, an additional mathematical tool is required: the density matrix operator ρ, or density matrix for short. For a quantum pure state $|\psi\rangle$, ρ is defined as the outer product of the state $|\psi\rangle\langle\psi|$. On the other hand, a mixed quantum state is defined as a state whose density matrix ρ_{MIX} is a linear combination (mixture) of the density matrix of pure quantum states $|\psi_X\rangle$, each contributing with a probability p_X [43]:

$$\rho_{MIX} = \sum_X p_X |\psi_X\rangle\langle\psi_X| \tag{A1}$$

Equation (A1) shows that the density state of a mixed state is not simply the outer product of the quantum state. Since the probabilities are normalized, $\sum_X p_X = 1$, Equation (A1) suggests that you can think of a quantum system in a pure state as an ensemble of quantum subsystems, all in the same pure quantum state.

Usually, quantum systems constituted by elementary subsystems exhibit non-separability (entanglement) [64]; the single elementary subsystems are therefore dubbed as entangled. The non-separability implies that the state of a quantum system with entanglement cannot be factorized in a tensorial product of pure quantum states. It is worth pointing out that if a composite quantum system with entanglement may be in a pure state, its single entangled subsystems are surely mixed [43]. The entanglement of each quantum subsystem with the rest of the quantum system, i.e., its environment, causes a loss of phase coherence, which, in turn, makes the state mixed. Therefore, a quantum gate exposed to the environment induces phase decoherence in the output state, which therefore results in a mixed state.

For a given mixed state, the pure entanglement quantum state, within which the mixed state is entangled, can be obtained through a procedure known as purification [38]. Since purification is essentially a reverse procedure, several entanglement pure states are possible for a given entangled mixed state. This remark explains the use of the maximum probability mentioned in the definition of Uhlmann's fidelity, introduced in Section 7.

Appendix B

The integrand quantities $|\alpha_i|^4$ and $|\alpha_i|^2|\alpha_j|^2$ in Equation (24) can be read as generated by the same product of a sequence:

$$\begin{aligned} |\alpha_i|^4 &= \prod_{h=1}^{k} |\alpha_h|^2 \\ |\alpha_i|^2|\alpha_j|^2 &= \prod_{h=1}^{k} |\alpha_h|^2 \end{aligned} \tag{A2}$$

with $k = 2$ and $\alpha_1 = \alpha_2 = \alpha_i$ for $|\alpha_i|^4$, and $\alpha_1 = \alpha_i$, $\alpha_2 = \alpha_j$ for $|\alpha_i|^2|\alpha_j|^2$. The two integrals in Equation (24) can therefore be traced back to one single integral:

$$\int_{S^{2n-1}} \prod_{h=1}^{k} |\alpha_h|^2 dV \tag{A3}$$

Because of the probability normalization condition on the component α_h:

$$\sum_{h=1}^{n} |\alpha_h|^2 = 1 \tag{A4}$$

the integral in Equation (A3) is carried out on a hypersphere of unitary radius. In addition, it should be also remarked that dV is the normalized infinitesimal Lebesgue measure on

the hypersphere. For calculating this integral, it is useful to address the following general integral defined in a r-dimensional complex vector space $\mathbb{C}^r$, whose generic vector z has components z_i:

$$\mathcal{I} = \int_{\mathbb{C}^r} e^{-|z|^2} \prod_{h=1}^{k} |z_h|^2 dV^r \tag{A5}$$

where dV^r is the infinitesimal Lebesgue measure in $\mathbb{C}^r$. It is worth noticing that, as in Equation (A2), Equation (A4) contains the product of a sequence of k terms, which, in the present case, are k components of a generic vector z instead of a state vector.

Figure A1 evidences that, in a two-dimensional vector space, the infinitesimal Lebesgue measure is the infinitesimal surface $d\sigma$, whose mathematical expression in polar coordinates is:

$$d\sigma = \rho d\rho d\varphi = \rho^{2-1} d\rho d\varphi_1 \tag{A6}$$

with $d\varphi_1 = d\varphi$, while in a three-dimensional vector space, it is the infinitesimal volume $d\tau$, whose mathematical expression in polar coordinates is:

$$d\tau = \rho d\theta \rho d\varphi d\rho = \rho^2 d\rho d\theta d\varphi = \rho^{3-1} d\rho \, d\varphi_1 d\varphi_2 \tag{A7}$$

with $d\varphi_1 = d\varphi$ and $d\varphi_2 = d\theta$.

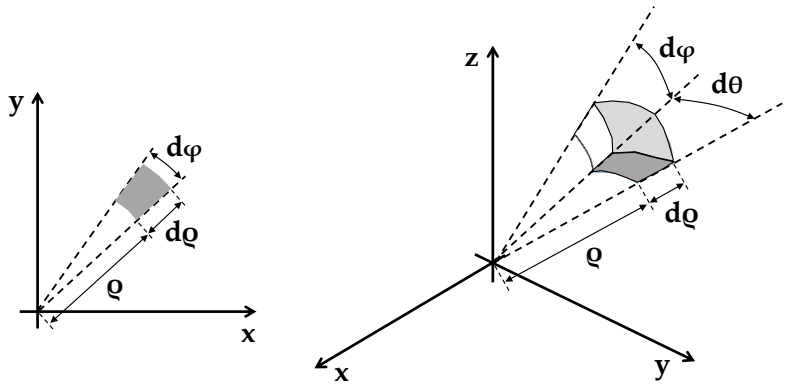

Figure A1. Infinitesimal Lebesgue measure in two- (**on the left**) and three-dimensional (**on the right**) vector spaces.

Equations (A6) and (A7) lead, by induction, to the following mathematical expression of dV:

$$dV^r = \rho^{2r-1} d\rho \prod_{j=1}^{2r-1} d\varphi_j \tag{A8}$$

A r-dimensional complex vector space $\mathbb{C}^r$ is indeed dimensionally equivalent to a 2r-dimensional real space. The substitution of Equation (A8) into Equation (A5) yields:

$$\mathcal{I} = \int_{S^{2r-1}} \int_0^\infty e^{-\rho^2} \prod_{h=1}^{k} |z_h|^2 \rho^{2r-1} d\rho \prod_{j=1}^{2r-1} d\varphi_j \tag{A9}$$

Inverting the integration order and separating the integration on ρ and φ_i yields:

$$\mathcal{I} = \int_0^\infty e^{-\rho^2} \rho^{2r-1} d\rho \int_{S^{2r-1}} \prod_{h=1}^{k} |z_h|^2 \prod_{j=1}^{2r-1} d\varphi_j \tag{A10}$$

since $\rho^2 = |z|^2$. The integral in $d\varphi_j$ is calculated in a hypersphere of radius $|z|$. Dividing and multiplying by $|z|^{2k}$ in the second integral leads to:

$$\mathcal{I} = \int_0^\infty e^{-\rho^2}\rho^{2r-1}d\rho \int_{S^{2r-1}} \prod_{h=1}^{k} |z|^{2k} \frac{|z_h|^2}{|z|^{2k}} \prod_{j=1}^{2r-1} d\varphi_j \tag{A11}$$

Since, as remarked above, $\rho^2 = |z|^2$, the term $|z|^{2k}$ can be repositioned into the integral in $d\rho$:

$$\mathcal{I} = \int_0^\infty e^{-\rho^2}\rho^{2k+2r-1}d\rho \int_{S^{2r-1}} \prod_{h=1}^{k} \frac{|z_h|^2}{|z|^{2k}} \prod_{j=1}^{2r-1} d\varphi_j \tag{A12}$$

In the product of a sequence in integral in $d\varphi_j$, the division by $|z|^{2k}$ is equivalent to dividing, by $|z|$, each $|z_h|$ term in the product, so that, by defining $\beta_h = z_h/z$, Equation (A12) takes the following form:

$$\mathcal{I} = \int_0^\infty e^{-\rho^2}\rho^{2k+2r-1}d\rho \int_{S^{2r-1}} |\beta_h|^2 \prod_{j=1}^{2r-1} d\varphi_j \tag{A13}$$

It is possible to remark that:

$$\sum_{h=1}^{r} |\beta_h|^2 = \sum_{h=1}^{r} \frac{|z_h|^2}{|z|^2} = \frac{\sum_{h=1}^{r}|z_h|^2}{|z|^2} = \frac{|z|^2}{|z|^2} = 1 \tag{A14}$$

because z_h are the components of z. The integral in $d\varphi_j$ in Equation (A13) is therefore calculated on a hypersphere of unitary radius as it is in the case of Equation (A3). Since dV is the normalized infinitesimal Lebesgue measure in Equation (A3), the normalization of the second integral to the surface Ω^{2r} of the unitary radius hypersphere makes this integral equal to Equation (A3):

$$\frac{\int_{S^{2r-1}} |\beta_h|^2 \prod_{j=1}^{2r-1} d\varphi_j}{\Omega^{2r}} = \int_{S^{2r-1}} \prod_{h=1}^{k} |\alpha_h|^2 dV \tag{A15}$$

The substitution of Equation (A15) into Equation (A13) yields:

$$\mathcal{I} = \Omega^{2r} \int_{S^{2r-1}} \prod_{h=1}^{k} |\alpha_h|^2 dV \int_0^\infty e^{-\rho^2}\rho^{2k+2r-1}d\rho \tag{A16}$$

Appendix C shows that in an n-dimensional real vector space $\mathbb{R}^n$, the surface Ω^n of the unitary radius hypersphere is given by:

$$\Omega^n = \frac{2\left(\sqrt{\pi}\right)^n}{\Gamma\left(\frac{n}{2}\right)} \tag{A17}$$

where Γ is Euler's gamma function:

$$\Gamma(z) = \int_0^\infty t^{z-1}e^{-t}dt \tag{A18}$$

Setting $n = 2r$ in Equation (A17) leads thus to the following mathematical expression of Ω^{2r}:

$$\Omega^{2r} = \frac{2\left(\sqrt{\pi}\right)^{2r}}{\Gamma(r)} = \frac{2\pi^r}{(r-1)!} \tag{A19}$$

where the property $\Gamma(n+1) = n!$ has been emphasized. The substitution of Equation (A19) into Equation (A16) yields:

$$\mathcal{I} = \frac{2\pi^r}{(r-1)!}\int_{S^{2r-1}}\prod_{h=1}^{k}|\alpha_h|^2 dV\int_0^\infty e^{-\rho^2}\rho^{2k+2r-1}d\rho \tag{A20}$$

Euler's gamma function also comes into play for calculating the integral in $d\rho$. By replacing ρ by $t^{1/2}$, Equation (A20) takes the following form:

$$\mathcal{I} = \frac{2\pi^r}{(r-1)!}\int_{S^{2r-1}}\prod_{h=1}^{k}|\alpha_h|^2 dV\int_0^\infty e^{-t}t^{\frac{2k+2r-1}{2}}\frac{1}{2\sqrt{t}}dt \tag{A21}$$

from which:

$$\mathcal{I} = \frac{2\pi^r}{(r-1)!}\frac{1}{2}\int_0^\infty e^{-t}t^{k+r-1}dt\int_{S^{2r-1}}\prod_{h=1}^{k}|\alpha_h|^2 dV \tag{A22}$$

The comparison of the integral in dt with Equation (A18) leads to the reformulation of Equation (A22) as follows:

$$\mathcal{I} = \frac{\pi^r}{(r-1)!}\Gamma(k+r)\int_{S^{2r-1}}\prod_{h=1}^{k}|\alpha_h|^2 dV = \frac{\pi^r(k+r-1)!}{(r-1)!}\int_{S^{2r-1}}\prod_{h=1}^{k}|\alpha_h|^2 dV \tag{A23}$$

where it is again emphasized that $\Gamma(n+1) = n!$. It is worth noting here that the aim of this appendix is to demonstrate the mathematical expression of the two integrals in Equation (24) that have been traced back to the integral in Equation (A3), which is in the right side of Equation (A23). To calculate this integral, you need to recalculate the integral $\mathcal{I}$ from Equation (A5), as performed for achieving Equation (A23), but in a different way. For this purpose, the integrand quantities $|\alpha_i|^4$ and $|\alpha_i|^2|\alpha_j|^2$ in Equation (24) have to be re-interpreted, not as in Equation (A2) but rather as follows:

$$\begin{aligned}|\alpha_i|^4 &= \prod_{h=1}^{r}|\alpha_h|^{2m_h}\\ |\alpha_i|^2|\alpha_j|^2 &= \prod_{h=1}^{r}|\alpha_h|^{2m_h}\end{aligned} \tag{A24}$$

where m_h is the multiplicity of the component α_h. It is worth noticing that, unlike in Equation (A2), Equation (A24) extends the product of a sequence over all of dimension r of the complex vector space; this compels us to introduce the multiplicity. As shown in Equation (A24), the new formulated product of a sequence generates $|\alpha_i|^4$ if $m_h = 2$ for $h = i$ and $m_h = 0$ otherwise, and $|\alpha_i|^2|\alpha_j|^2$ if $m_h = 1$ for $h = i = j$ and $m_h = 0$ otherwise. Following Equation (A24), Equation (A5) takes the following form:

$$\mathcal{I} = \int_{\mathbb{C}^r} e^{-|z|^2}\prod_{h=1}^{r}|z_h|^{2m_h}dV^r \tag{A25}$$

It is now possible to remark that:

$$\begin{aligned}|z|^2 &= \sum_{h=1}^{r}|z_h|^2\\ dV^r &= \prod_{h=1}^{r}dz_h\end{aligned} \tag{A26}$$

The substitution of Equation (A26) into Equation (A25) yields:

$$\mathcal{I} = \int_{\mathbb{C}^r} \prod_{h=1}^{r} e^{-|z_h|^2} |z_h|^{2m_h} dz_h = \prod_{h=1}^{r} \int_{\mathbb{C}^1} e^{-|z_h|^2} |z_h|^{2m_h} dz_h \tag{A27}$$

In this way, the integral in the r-dimensional complex vector space $\mathbb{C}^r$ has been reduced to the product of a sequence of integrals in the one-dimensional complex vector space $\mathbb{C}^1$. Because the dimension is one, in this space, z_h is the unique vector and dz_h is the infinitesimal Lebesgue measure. In polar coordinates, it holds therefore that $|z_h| = \rho$. In addition, Equation (A6) provides the mathematical expression of the infinitesimal Lebesgue measure, because a one-dimensional complex vector space $\mathbb{C}^1$ is dimensionally equivalent to a two-dimensional real vector space. It holds therefore that $dz_h = \rho d\rho d\varphi$. Consequently, Equation (A27) can be reformulated as follows:

$$\mathcal{I} = \prod_{h=1}^{r} \int_{\mathbb{C}^1} e^{-\rho^2} \rho^{2m_h} \rho d\rho d\varphi = \prod_{h=1}^{r} \int_0^{2\pi} \int_0^{\infty} e^{-\rho^2} \rho^{2m_h} \rho d\rho d\varphi \tag{A28}$$

from which:

$$\mathcal{I} = \prod_{h=1}^{r} \int_0^{2\pi} d\varphi \int_0^{\infty} e^{-\rho^2} \rho^{2m_h+1} d\rho = (2\pi)^r \prod_{h=1}^{r} \int_0^{\infty} e^{-\rho^2} \rho^{2m_h+1} d\rho \tag{A29}$$

The integral in ρ can be calculated by setting $\rho = t^{1/2}$, as done for Equation (A20). In this way, you obtain:

$$\mathcal{I} = \frac{(2\pi)^r}{2^r} \prod_{h=1}^{r} \int_0^{\infty} e^{-t} \rho^{m_h} dt = \frac{(2\pi)^r}{2^r} \prod_{h=1}^{r} \int_0^{\infty} e^{-t} \rho^{(m_h+1)-1} dt = \pi^r \prod_{h=1}^{r} \Gamma(m_h + 1) \tag{A30}$$

Since $\Gamma(\mathrm{n}+1) = \mathrm{n}!$, Equation (A30) takes the following short form:

$$\mathcal{I} = \pi^r \prod_{h=1}^{r} m_h! \tag{A31}$$

The substitution of Equation (A31) into Equation (A23) yields:

$$\pi^r \prod_{h=1}^{r} m_h! = \frac{\pi^r (k+r-1)!}{(r-1)!} \int_{S^{2r-1}} \prod_{h=1}^{k} |\alpha_h|^2 dV \tag{A32}$$

from which:

$$\int_{S^{2r-1}} \prod_{h=1}^{k} |\alpha_h|^2 dV = \frac{(r-1)!}{\pi^r (k+r-1)!} \pi^r \prod_{h=1}^{r} m_h! = \frac{(r-1)!}{(k+r-1)!} \prod_{h=1}^{r} m_h! \tag{A33}$$

From the definition of k in Equation (A2) and of m_h in Equation (A24), it holds that:

$$\begin{aligned} k &= \sum_{j=1}^{r} m_j \\ \int_{S^{2r-1}} \prod_{h=1}^{k} |\alpha_h|^2 dV &= \int_{S^{2r-1}} \prod_{h=1}^{r} |\alpha_h|^{2m_h} dV \end{aligned} \tag{A34}$$

By observing that $|\alpha_h|^4$ can be interpreted as a product of vector components α_j with $m_j = 2$, if $j = h$ and $m_j = 0$ if $j \neq h$, you can write:

$$\begin{aligned} \sum_{j=1}^{r} m_j &= 2 \\ \prod_{j=1}^{r} m_j! &= 2 \end{aligned} \tag{A35}$$

The substitution of Equations (A34) and (A35) into Equation (A33) yields:

$$\int_{S^{2r-1}} |\alpha_i|^4 dV = \frac{(r-1)!}{(2+r-1)!} 2 = \frac{2(r-1)!}{(r+1)!} = \frac{2}{r(r+1)} \tag{A36}$$

Similarly, since, Equation (A24) generates $|\alpha_i|^2 |\alpha_j|^2$ if $m_h = 1$ for $h = i = j$ and $m_h = 0$ otherwise, you get:

$$\begin{aligned} \sum_{j=1}^{r} m_j &= 2 \\ \prod_{j=1}^{r} m_j! &= 1 \end{aligned} \tag{A37}$$

The substitution of Equations (A34) and (A37) into Equation (A33) yields:

$$\int_{S^{2r-1}} |\alpha_i|^2 |\alpha_j|^2 dV = \frac{(r-1)!}{(2+r-1)!} = \frac{1}{r(r+1)} \tag{A38}$$

Equations (A36) and (A38) demonstrate Equation (24).

Appendix C

By extending the Gaussian integral on a one-dimensional real vector space $\mathbb{R}^1$:

$$\int_{\mathbb{R}^1} e^{-\frac{|x_1|^2}{2}} dx_1 = \sqrt{2\pi} \tag{A39}$$

to a n-dimensional real vector space $\mathbb{R}^n$, you obtain:

$$\int_{\mathbb{R}^n} e^{-\frac{|x|^2}{2}} dx = \int_{\mathbb{R}^n} \prod_{h=1}^{n} e^{-\frac{|x_h|^2}{2}} dx_h = \prod_{h=1}^{n} \int_{\mathbb{R}^1} e^{-\frac{|x_h|^2}{2}} dx_h = \prod_{h=1}^{n} \sqrt{2\pi} = \left(\sqrt{2\pi}\right)^n \tag{A40}$$

Following the calculation procedure adopted for Equation (A9), the integral in dx in Equation (A40) can be calculated by means of the polar coordinates as follows:

$$\int_{\mathbb{R}^n} e^{-\frac{|x|^2}{2}} dx = \int_{S^{n-1}} \int_0^\infty e^{-\frac{\rho^2}{2}} \rho^{n-1} d\rho \prod_{j=1}^{n-1} d\varphi_j = \int_{S^{n-1}} \prod_{j=1}^{n-1} d\varphi_j \int_0^\infty e^{-\frac{\rho^2}{2}} \rho^{n-1} d\rho \tag{A41}$$

The integral in $d\varphi_j$ is the surface Ω^n of a unitary radius hypersphere in the $\mathbb{R}^n$ vector space. The radius does not appear in the integral, indicating that it is unitary. Equation (A41) can be therefore rewritten as follows:

$$\int_{\mathbb{R}^n} e^{-\frac{|x|^2}{2}} dx = \Omega^n \int_0^\infty e^{-\frac{\rho^2}{2}} \rho^{n-1} d\rho \tag{A42}$$

The integral in $d\rho$ can be calculated by replacing ρ by $(2t)^{1/2}$:

$$\int_{\mathbb{R}^n} e^{-\frac{|x|^2}{2}} dx = \Omega^n \int_0^\infty e^{-\frac{2t}{2}} (2t)^{\frac{n-1}{2}} \frac{1}{2} \frac{2}{\sqrt{2t}} dt = \Omega^n \int_0^\infty e^{-t} (2t)^{\frac{n}{2}-1} dt \tag{A43}$$

from which:

$$\int_{\mathbb{R}^n} e^{-\frac{|x|^2}{2}} dx = \Omega^n 2^{\frac{n}{2}-1} \int_0^\infty e^{-t} t^{\frac{n}{2}-1} dt \tag{A44}$$

The comparison with Equation (A18) shows that the integral on the right-hand side of Equation (A44) is $\Gamma(n/2)$, and thus Equation (A44) takes the following form:

$$\int_{\mathbb{R}^n} e^{-\frac{|x|^2}{2}} dx = \Omega^n 2^{\frac{n}{2}-1} \Gamma\left(\frac{n}{2}\right) \tag{A45}$$

from which:

$$\Omega^n = \frac{\int_{\mathbb{R}^n} e^{-\frac{|x|^2}{2}} dx}{2^{\frac{n}{2}-1}\Gamma\left(\frac{n}{2}\right)} \tag{A46}$$

The substitution of Equation (A40) into Equation (A46) yields:

$$\Omega^n = \frac{\left(\sqrt{2\pi}\right)^n}{2^{\frac{n}{2}-1}\Gamma\left(\frac{n}{2}\right)} = 2\frac{2^{\frac{n}{2}}\pi^{\frac{n}{2}}}{2^{\frac{n}{2}}\Gamma\left(\frac{n}{2}\right)} = 2\frac{\left(\sqrt{\pi}\right)^n}{\Gamma\left(\frac{n}{2}\right)} \tag{A47}$$

which demonstrates Equation (A17).

References

1. Chang, C.R.; Wang, M.C. *Tiny Quantum, Giant Revolution*; World Scientific Publishing Company: Singapore, 2024; ISBN 978-9811287404.
2. Peng, Y.; Benserhir, J.; Zou, Y.; Charbon, E. A Cryogenic Double-IF SSB Controller with Image Suppression and On-Chip Filtering implemented in 130nm SiGe BiCMOS Technology for Superconducting Qubit Control. In Proceedings of the 2024 IEEE Custom Integrated Circuits Conference (CICC), Denver, CO, USA, 21–24 April 2024; pp. 32–34. [CrossRef]
3. Chakraborty, S.; Tien, K.; Frolov, D.; Frank, D.; Rosno, P.; Yeck, M.; Bulzacchelli, J.; Baks, C.; Richetta, R.; Schmerbeck, T.; et al. A 12.8mW/channel cryogenic RF-AWG in 14nm FinFET for transmon qubit control. In Proceedings of the 2024 IEEE European Solid-State Electronics Research Conference (ESSERC), Bruges, Belgium, 9–12 September 2024; pp. 153–156. [CrossRef]
4. Chakraborty, S.; Joshi, R.V. Cryogenic CMOS Design for Qubit Control: Present Status, Challenges, and Future Directions. *IEEE Circuits Syst. Mag.* **2024**, *24*, 34–36. [CrossRef]
5. Badiali, A.; Borgarino, M. Cryo-CMOS Multi-Frequency Modulator for 2-Qubit Controller. *Electronics* **2024**, *13*, 2546. [CrossRef]
6. Anders, J.; Babaie, M.; Bardin, J.C.; Bashir, I.; Billiot, G.; Blokhina, E.; Bonen, S.; Charbon, E.; Chiaverini, J.; Chuang, I.L.; et al. CMOS Integrated Circuits for the Quantum Information Sciences. *IEEE Trans. Quantum Eng.* **2023**, *4*, 5100230. [CrossRef]
7. Frank, D.J.; Chakraborty, S.; Tien, K.; Rosno, P.; Yeck, M.; Glick, J.A.; Robertazzi, R.; Richetta, R.; Bulzacchelli1, J.F.; Ramirez, D.; et al. Low power cryogenic RF ASICs for quantum computing. In Proceedings of the IEEE Custom Integrated Circuits Conference (CICC), San Antonio, TX, USA, 23–26 April 2023. [CrossRef]
8. Guo, Y.; Li, Y.; Huang, W.; Tan, S.; Liu, Q.; Li, T.; Deng, N.; Wang, Z.; Zheng, Y.; Jiang, H. A Polar-Modulation-Based Cryogenic Qubit State Controller in 28nm Bulk CMOS. In Proceedings of the IEEE International Solid-State Circuits Conference (ISSCC), San Francisco, CA, USA, 19–24 February 2023; pp. 508–510. [CrossRef]
9. Kang, K.; Minn, D.; Lee, J.; Song, H.-J.; Lee, M.; Sim, J.-Y. A Cryogenic Controller IC for Superconducting Qubits with DRAG Pulse Generation by Direct Synthesis without Using Memory. In Proceedings of the IEEE International Solid-State Circuits Conference (ISSCC), San Francisco, CA, USA, 19–24 February 2023; pp. 510–512. [CrossRef]
10. Yoo, J.; Chen, Z.; Arute, F.; Montazeri, S.; Szalay, M.; Erickson, C.; Jeffrey, E.; Fatemi, R.; Giustina, M.; Ansmann, M.; et al. A 28-nm Bulk-CMOS IC for Full Control of a Superconducting. Quantum Processor Unit-Cell. In Proceedings of the IEEE International Solid-State Circuits Conference (ISSCC), San Francisco, CA, USA, 19–24 February 2023; pp. 506–508. [CrossRef]
11. Omirzakhov, K.; Idjadi, M.H.; Huang, T.Y.; Breitweiser, S.A.; Hopper, D.A.; Bassett, L.C.; Aflatouni, F. An Integrated Reconfigurable Spin Control System on 180 nm CMOS for Diamond NV Centers. *IEEE Trans. Microw. Theory Technol.* **2023**, *71*, 4052–4063. [CrossRef]
12. Omirzakhov, K.; Idjadi, M.H.; Huang, T.-Y.; Breitweiser, S.A.; Hopper, D.A.; Bassett, L.C.; Aflatouni, F. An Integrated Quantum Spin Control System in 180nm CMOS. In Proceedings of the IEEE Radio Frequency Integrated Circuits (RFIC) Symposium, Denver, CO, USA, 19–21 June 2022; pp. 36–43. [CrossRef]
13. Kang, K.; Minn, D.; Bae, S.; Lee, J.; Kang, S.; Lee, M.; Song, H.-J.; Sim, J.-Y. A 40-nm Cryo-CMOS Quantum Controller IC for Superconducting Qubit. *IEEE J. Solid-State Circuits* **2022**, *57*, 3274–3287. [CrossRef]
14. Frank, D.J.; Chakraborty, S.; Tien, K.; Rosno, P.; Fox, T.; Yeck, M.; Glick, J.A.; Robertazzi, R.; Richetta, R.; Bulzacchelli, J.F.; et al. A Cryo-CMOS Low-Power Semi-Autonomous Qubit State Controller in 14nm FinFET Technology. In Proceedings of the IEEE International Solid- State Circuits Conference (ISSCC), San Francisco, CA, USA, 20–26 February 2022; pp. 360–362. [CrossRef]

15. Nikandish, R.; Blokhina, E.; Leipold, D.; Staszewski, R.B. Semiconductor Quantum Computing: Toward a CMOS quantum computer on chip. *IEEE Nanotechnol. Mag.* **2021**, *15*, 8–20. [CrossRef]
16. Park, J.-S.; Subramanian, S.; Lampert, L.; Mladenov, T.; Klotchkov, I.; Kurian, D.J.; Juarez-Hernandez, E.; Perez-Esparza, B.; Kale, S.R.; Asma Beevi, K.T.; et al. A Fully Integrated Cryo-CMOS SoC for Qubit Control in Quantum Computers Capable of State Manipulation, Readout and High-Speed Gate Pulsing of Spin Qubits in Intel 22nm FFL FinFET Technology. In Proceedings of the IEEE International Solid- State Circuits Conference (ISSCC), San Francisco, CA, USA, 3 March 2021; pp. 208–210. [CrossRef]
17. Hasler, J.; Dick, N.; Das, K.; Degnan, B.; Moini, A.; Reilly, D. Cryogenic Floating-Gate CMOS Circuits for Quantum Control. *IEEE Trans. on Quantum Eng.* **2021**, *2*, 5501510. [CrossRef]
18. Pauka, S.J.; Das, K.; Kalra, R.; Moini, A.; Yang, Y.; Trainer, M.; Bousquet, A.; Cantaloube, C.; Dick, N.; Gardner, G.C.; et al. A cryogenic CMOS chip for generating control signals for multiple qubits. *Nat. Electron.* **2021**, *4*, 64–70. [CrossRef]
19. Charbon, E. Cryo-CMOS Electronics for Quantum Computing. *IEEE Solid-State Circuits Mag.* **2021**, *13*, 54–68. [CrossRef]
20. Bardin, J.C. A Low-Power CMOS Quantum Controller for Transmon Qubits. In Proceedings of the IEEE International Electron Devices Meeting (IEDM), San Francisco, CA, USA, 12–18 December 2020; pp. 537–540. [CrossRef]
21. Craninckx, J.; Potočnik, A.; Parvais, B.; Grill, A.; Narasimhamoorthy, S.; Van Winckel, S.; Brebels, S.; Mongillo, M.; Li, R.; Govoreanu, B.; et al. CMOS Cryo-Electronics for Quantum Computing. In Proceedings of the IEEE International Electron Devices Meeting (IEDM), San Francisco, CA, USA, 12–18 December 2020; pp. 521–524. [CrossRef]
22. Borgarino, M.; Badiali, A. Quantum Gates for Electronics Engineers. *Electronics* **2023**, *12*, 4664. [CrossRef]
23. Bardin, J.C.; Slichter, D.H.; Reilly, D.J. Microwaves in Quantum Computing. *IEEE J. Microw.* **2021**, *1*, 403–427. [CrossRef] [PubMed]
24. Sanders, Y.R.; Wallman, J.J.; Sanders, B.C. Bounding quantum gate error rate based on reported average fidelity. *IOP Dtsch. Phys. Ges. New J. Phys.* **2016**, *18*, 012002. [CrossRef]
25. Devitt, S.J.; Munro, W.J.; Nemoto, K. Quantum error correction for beginners. *IOP Rep. Prog. Phys.* **2013**, *76*, 076001. [CrossRef] [PubMed]
26. Nielsen, M.A.; Chuang, I.L. *Quantum Computation and Quantum Information*, 10th ed.; Cambridge University Press: Cambridge, UK, 2010; ISBN 978-1-107-00217-3.
27. Benhelm, J.; Kirchmair, G.; Roos, C.F.; Blatt, R. Towards fault-tolerant quantum computing with trapped ions. *Nat. Phys.* **2008**, *4*, 463–466. [CrossRef]
28. Van Dijk, J.P.G.; Kawakami, E.; Schouten, R.N.; Veldhorst, M.; Vandersypen, L.M.K.; Babaie, M.; Charbon, E.; Sebastiano, F. Impact of Classical Control Electronics on Qubit Fidelity. *Phys. Rev. Applied* **2019**, *12*, 044054. [CrossRef]
29. Ferraro, E.; Fanciulli, M.; De Michielis, M. Gate fidelity comparison in semiconducting spin qubit implementations affected by control noises. *IOP J. Phys. Commun.* **2018**, *2*, 115022. [CrossRef]
30. Fakkel, N.; Enthoven, L.; Yun, J.; Van Riggelen, M.; Van Ommen, H.B.; Schymik, K.-N.; Bartling, H.P.; Katranara, E.T.; Vollmer, R.; Taminiau, T.H.; et al. A Cryo-CMOS Controller with Class-DE Driver and DC Magnetic-Field Tuning for Quantum Computers Based on Color Centers in Diamond. *IEEE J. Solid-State Circuits* **2024**, *59*, 3627–3643. [CrossRef]
31. Tyryshkin, A.; Tojo, S.; Morton, J.L.; Riemann, H.; Abrosimov, N.V.; Becker, P.; Pohl, H.-J.; Schenkel, T.; Thewalt, M.L.W.; Itoh, K.M.; et al. Electron spin coherence exceeding seconds in high-purity silicon. *Nat. Mater.* **2012**, *11*, 143–147. [CrossRef]
32. Pedersen, L.H.; Møller, N.M.; Mølmer, K. Fidelity of quantum operations. *Elsevier Phys. Lett. A* **2007**, *367*, 47–51. [CrossRef]
33. Bruß, D.; DiVincenzo, D.P.; Ekert, A.; Fuchs, C.A.; Macchiavello, C.; Smolin, J.A. Optimal universal and stae-dependent quantum cloning. *APS Phys. Rev. A* **1998**, *57*, 2368–2378. [CrossRef]
34. Bowdrey, A.D.; Oi, D.K.L.; Short, A.J.; Banaszek, K.; Jones, J.A. Fidelity of single qubit maps. *Elsevier Phys. Lett. A* **2002**, *294*, 258–260. [CrossRef]
35. Baldwin, A.J.; Jones, J.A. Efficiently computing the Uhlmann fidelity for density matrices. *APS Phys. Rev. A* **2023**, *107*, 012427. [CrossRef]
36. Shannon, C.E. A Mathematical Theory of Communication. *Bell Syst. J.* **1948**, *27*, 379–423. [CrossRef]
37. Evered, S.J.; Bluvstein, D.; Kalinowski, M.; Ebadi, S.; Manovitz, T.; Zhou, H.; Li, S.H.; Geim, A.A.; Wang, T.T.; Maskara, N.; et al. High-fidelity parallel entangling gates on a neutral-atom quantum computer. *Nature* **2023**, *622*, 268–272. [CrossRef] [PubMed]
38. Wilde, W. *Quantum Information Theory*, 2nd ed.; Cambridge University Press: Cambridge, UK, 2017; ISBN 978-1107176164.
39. Kemp, C.J.D.; Cooper, N.R.; Ünal, F.N. Nested-sphere description of the N-level Chern number and the generalized Bloch hypersphere. *APS Phys. Rev. Res.* **2022**, *4*, 023120. [CrossRef]
40. Dirac, P.A.M. *The Principle of Quantum Mechanics*, 4th ed.; Clarendon Press: Oxford, UK, 1958; ISBN 978-0198512080.
41. Horn, R.A.; Johnson, C.R. *Matrix Analysis*, 2nd ed.; Cambridge University Press: Cambridge, UK, 2013; ISBN 978-0521548236.
42. Zettili, N. *Quantum Mechanics*, 3rd ed.; Wiley & Sons: Hoboken, NJ, USA, 2022; ISBN 9781118307892.
43. Susskind, L.; Friedman, A. *Quantum Mechanics: The Theoretical Minimum*, 1st ed.; Penguin Books Ltd.: London, UK, 2014; ISBN 978-0141977812.
44. Merzbacher, E. *Quantum Mechanics*, 2nd ed.; Wiley & Sons: Hoboken, NJ, USA, 1997; ISBN 978-0471887027.

45. Horodecki, M.; Horodecki, P.; Horodecki, R. General teleportation channel, singlet fraction, and quasidistillation. *APS Phys. Rev. A* **1999**, *60*, 1888–1898. [CrossRef]
46. Barends, R.; Kelly, J.; Megrant, A.; Veitia, A.; Sank, D.; Jeffrey, E.; White, T.C.; Mutus, J.; Fowler, A.G.; Campbell, B.; et al. Superconducting quantum circuits at the surface code threshold for fault tolerance. *Nature* **2014**, *508*, 500–503. [CrossRef]
47. AbuGhanem, M.; Eleuch, J. Full quantum tomography study of Google's Sycamore gate on IBM's quantum computers. *EPJ Quantum Technol.* **2024**, *11*, 36. [CrossRef]
48. Rower, D.A.; Ding, L.; Zhang, H.; Hays, M.; An, J.; Harrington, P.M.; Rosen, I.T.; Gertler, J.M.; Hazard, T.M.; Niedzielski, B.M.; et al. Suppressing Counter-Rotating Errors for Fast Single-Qubit Gates with Fluxonium. *Am. Phys. Soc. PRX Quantum.* **2024**, *5*, 040342. [CrossRef]
49. Dehollain, J.P.; Muhonen, J.T.; Blume-Kohout, R.; Rudinger, K.M.; Gamble, J.K.; Nielsen, E.; Laucht, A.; Simmons, S.; Kalra, R.; Dzurak, A.S.; et al. Optimization of a solid-state electron spin qubit using gate set tomography. *IOP Dtsch. Phys. Ges. New J. Phys.* **2016**, *18*, 103018. [CrossRef]
50. Tannu, S.S.; Qureshi, M.K. Not All Qubits Are Created Equal: A Case for Variability-Aware Policies for NISQ-Era Quantum Computers. In Proceedings of the 24th International Conference on Architectural Support for Programming Languages and Operating Systems (ASPLOS), Providence, RI, USA, 13–17 April 2019; pp. 987–999. [CrossRef]
51. Quantum error correction below the surface code threshold. *Nature* **2024**. [CrossRef]
52. Ikonen, J.; Salmilehto, J.; Möttönen, M. Energy-efficient quantum computing. *NPJ Quantum Inf.* **2017**, *3*, 17. [CrossRef]
53. Auffèves, A. Quantum Technologies Need a Quantum Energy Initiative. *Am. Phys. Soc. PRX Quantum* **2022**, *3*, 020101. [CrossRef]
54. Huang, J.Y.; Su, R.Y.; Lim, W.H.; Feng, M.; Van Straaten, B.; Severin, B.; Gilbert, W.; Stuyck, N.D.; Tanttu, T.; Serrano, S.; et al. High-fidelity spin qubit operation and algorithmic initialization above 1 K. *Nature* **2024**, *627*, 772–777. [CrossRef] [PubMed]
55. Bialczak, R.C.; Ansmann, M.; Hofheinz, M.; Lucero, E.; Neeley, M.; O'Connell, A.D.; Sank, D.; Wang, H.; Wenner, J.; Steffen, M.; et al. Quantum process tomography of a universal entangling gate implemented with Josephson phase qubits. *Nat. Phys.* **2010**, *6*, 409–413. [CrossRef]
56. Nielsen, M.A. A simple formula for the average gate fidelity of quantum dynamical operation. *Elsevier Phys. Lett. A* **2002**, *303*, 249–252. [CrossRef]
57. Życzkowski, K.; Sommers, H.-J. Average fidelity between random quantum states. *APS Phys. Rev. A* **2005**, *71*, 032313. [CrossRef]
58. Uhlmann, A. The transition probability in the state space of a *-algebra. *Rep. Math. Phys.* **1976**, *9*, 273–279. [CrossRef]
59. Jozsa, R. Fidelity for mixed quantum states. *J. Mod. Opt.* **1994**, *12*, 2315–2323. [CrossRef]
60. O'Brien, J.L.; Pryde, G.J.; Gilchrist, A.; James, D.F.; Langford, N.K.; Ralph, T.C.; White, A.G. Quantum Process Tomography of a Controlled-NOT Gate. *Phys. Rev. Lett.* **2004**, *93*, 080502. [CrossRef]
61. Koutromanos, D.; Stefanatos, D.; Paspalakis, E. Control of Qubit Dynamics Using Reinforcement Learning. *Information* **2024**, *15*, 272. [CrossRef]
62. Bonizzoni, C.; Tincani, M.; Santanni, F.; Affronte, M. Machine-Learning-Assisted Manipulation and Readout of Molecular Spin Qubits. *Phys. Rev. Appl.* **2022**, *18*, 064074. [CrossRef]
63. Zurek, W.H. Decoherence and the Transition from Quantum to Classical—Revisited. *Prog. Math. Phys.* **2006**, *48*, 86–109. [CrossRef]
64. Marcella, T.V. *Quantum Entanglement and the Loss of Reality*, 1st ed.; Createspace Independent Publishing Platform: Scotts Valley, CA, USA, 2018; ISBN 978-1981807420.